



Tailoring the Microstructure using Quenching and Partitioning Processing in a Commercial Mn-Si-Cr Spring Steel to Improve Tensile Properties

Mohammad Masoumi¹ · Dany Michell Andrade Centeno² · Edwan Anderson Ariza Echeverri³

Received: 22 November 2023 / Accepted: 20 February 2024
© The Author(s) 2024

Abstract

This study explores a novel approach to quenching and partitioning (Q&P) heat treatment applied to AISI 9260 spring steel, comprising Fe-0.65C-1.58Mn-1.05Si-0.41Cr (wt.%). Our research focuses on balancing strength and ductility through optimized Q&P pathways, leading to a diverse microstructure that includes martensite, bainite, carbide, and retained austenite. Advanced X-ray diffraction and scanning electron microscopy techniques were employed to analyze the complexities of this microstructure. A key aspect of this study is the precise control of partitioning temperature and time, crucial for modulating lattice distortion and dislocation density within martensitic and bainitic structures. Optimal partitioning temperature promotes carbon distribution into austenite, tempering lattice distortions, and dislocation densities. Concurrently, carbide precipitation and segregation contribute to the refinement of the bainite phase. The sample quenched at 125 °C and partitioned at 350 °C (Q&P-125/350) demonstrates notable mechanical properties: a yield strength of 950 ± 15 MPa, an ultimate tensile strength of 1710 ± 15 MPa, and an elongation of approximately 9.7%. These results are partly attributed to the effect of silicon in preventing cementite coarsening and the effective distribution of carbide. Our findings highlight the potential of Q&P heat treatment in developing tailored microstructures with enhanced mechanical properties in steel, without relying on costly alloying elements. This approach presents new avenues for the design and application of high-performance materials.

Keywords Quenching and Partitioning · Commercial pearlitic steel · Microstructure · Tensile behavior · EBSD

1 Introduction

The transportation industry is in urgent need of rapid improvements and sustained advancements in ultra-high-strength steels (UHSS), coupled with reductions in energy consumption and carbon emissions. As a result, there has been a notable increase in research aimed at discovering

innovative material compositions and processing methods. The objectives are to maintain high strength and formability of these materials and to gain a thorough understanding of the underlying science through practical experimentation.

Bainitic steels are particularly favored across various industries due to their combined strength and flexibility. The quenching and partitioning (Q&P) process is employed to produce a new generation of advanced high-strength steel (AHSS), which exhibits enhanced ductility owing to the presence of untransformed austenite [1, 2]. Silicon, when added to the steel composition, helps suppress the formation of carbides. This increases the stability of fine interlath untransformed austenite and bolsters both the transformation-induced plasticity (TRIP) effect and fracture toughness [3, 4].

The high silicon content of commercial carbon-silicon spring steel is of significant interest due to the potential for obtaining a complex microstructure composed of bainitic-ferrite and retained austenite. The primary objective of Q&P

✉ Mohammad Masoumi
mohammad.m@ufabc.edu.br

✉ Edwan Anderson Ariza Echeverri
earizaec@unimagdalena.edu.co

¹ Centro de Engenharia, Modelagem e Ciências Sociais Aplicadas, Universidade Federal do ABC, Santo André, SP 09210-580, Brazil

² Metallurgical Processes Laboratory, Institute for Technological Research, Av. Prof. Almeida Prado, São Paulo 532, Brazil

³ Grupo de Nuevos Materiales, Facultad de Ingeniería, Universidad del Magdalena, Santa Marta, Colombia



process is to develop a sophisticated multiphase microstructure, predominantly characterized by martensite and retained austenite, with occasional presence of bainite. These phases synergistically enhance the mechanical properties of the material. The Q&P process has piqued the interest of metallurgists and the broader manufacturing sector, as it offers a pathway to develop high-strength steels that maintain significant ductility, eliminating the need for complex alloying. The addition of 1–2 wt% silicon into the steel composition increases austenite stability and inhibits carbide precipitation, resulting in a larger fraction of retained austenite [5, 6]. Austempering of high-Si, low-alloy steel for 20 h at 250 °C, followed by gas quenching, resulted in complex martensitic and nanobainitic microstructures devoid of precipitated carbides [7]. Partitioning applied to Fe-0.4C-1.05Si (wt%) steel, at 300 °C for 1000 s, led to the precipitation of η -carbides within the martensite laths, leaving approximately 18% of retained austenite in the microstructure of the steel in question [8]. Control over the volume fractions of martensite, bainite, transition carbides, and retained austenite in the microstructure facilitates tailoring a wide range of mechanical properties of steels. Carbon-silicon spring steel, utilized in the manufacturing of various components, has garnered attention due to the complex microstructures of bainitic-ferrite and retained austenite achieved by its high Si content. Masoumi et al. [9] developed a microstructure consisting of a dispersion of transition carbides throughout tempered martensite and bainitic-ferrite, which displayed ultra-high strength, with reasonable ductility and good toughness in commercial pearlitic steel (AISI 1070). Although quantifying complex microstructures remains a challenge, the development of complex microstructures that bridge the gap between chemical composition and thermomechanical processing is critical for attaining optimized mechanical properties.

Q&P steels have undergone extensive study in recent years [5–9]. However, the interplay between different transformation mechanisms can result in intricate microstructures. These microstructures consist of tempered martensite, carbides, bainite, retained austenite, and freshly formed martensite, all of which present challenges in controlling the resulting properties. AISI 9260 spring steel is widely used in manufacturing heavy-duty springs for diverse applications, encompassing automotive suspension systems, agricultural machinery, and industrial equipment. Due to its high silicon content, modern Q&P processing techniques could potentially enable more precise control and optimization of the complex microstructures in this type of steel. In turn, this could enhance mechanical properties such as strength and toughness, yielding substantial improvements. Such advancements could significantly impact industrial applications by offering more durable and reliable heavy-duty

springs, which is a promising prospect, particularly for sectors like automotive and agriculture.

Dalwatkar et al. [10] explored the impact of austempering on SAE 9260 steel, highlighting the increase in retained austenite with higher isothermal transformation temperatures and its correlation with enhanced strength and ductility. In a different context, the investigation of Yan et al. [11] into the failure of an automobile spring made of similar steel underscores the importance of microstructural integrity in real-world applications. Hasanlou et al. [12] examined the fracture and hardening behaviors of TRIP steel under various heat treatments, revealing insights into the microstructural, mechanical, and fracture properties of these steels. Studies by Masoumi et al. [13–15] on AISI 9254 steel further underscore the potential of the Q&P process in achieving high-strength and ductile steel, with a focus on the role of silicon in preventing carbide coalescence and enhancing strain-hardening capacity. These findings collectively demonstrate the evolving landscape of steel processing and the critical role of heat treatment techniques like Q&P in achieving desired mechanical properties.

The steel is first heated to an austenitizing temperature, typically between 830 and 870 °C, and held at this temperature for a specific time to dissolve the alloying elements. It is then quenched in oil or water to rapidly transform the austenite into martensite. After quenching, the steel is tempered at a lower temperature to relieve internal stresses and improve toughness and ductility. This tempering temperature and time can be determined based on the desired material properties. Additionally, AISI 9260 steel frequently undergoes cold working operations, such as coiling helicoid springs, rolling, or drawing. These operations demand ductility and a reasonable difference between the yield and ultimate strengths, also known as the elastic ratio. Typically, the hardness of this steel ranges from 321–375 HV, yield stress spans 690–1200 MPa, and the ultimate tensile strength lies between 925–1860 MPa [16–18].

In this study, we selected 1.05 wt.% Si in our steel composition to explore its influence on cementite coarsening and carbon partitioning in bainitic structures. This specific Si content was chosen based on a comprehensive review of the literature [19–22], which suggests that while higher Si levels (above 1.5 wt.%) can lead to significant alterations in carbide formation and bainitic transformation kinetics, levels around 1.05 wt.% can effectively retard cementite coarsening without drastically altering the fundamental characteristics of the bainitic transformation. This concentration allows us to investigate the nuanced impact of Si on the microstructure, particularly in terms of carbon partitioning and the stability of retained austenite, without the extreme effects observed at higher Si levels. The choice is a deliberate balance, aimed at understanding the subtle interplay between Si content and

the microstructural evolution in bainitic steels, which is crucial for optimizing their mechanical properties and industrial applicability.

In this study, we aim to pave for the development of high-performance Mn-Si-Cr steels through an innovative Q&P heat treatment process. Our objectives involve leveraging Q&P to engineer a finely tuned multiphase microstructure that delivers superior strength and ductility and scrutinize the influence of partitioning temperature and time on lattice distortions and internal stress levels during the martensitic transformation. We utilized dilatometry to track dimensional changes, a process indicative of phase transformations, and employed advanced metallography and microscopy techniques, including SEM and EBSD, to visualize microstructural and crystallographic evolutions. Moreover, we aim to decipher the role of silicon in suppressing cementite coarsening and to elucidate the influence of carbon partitioning and carbide precipitation on the characteristics of bainitic structures. Ultimately, we endeavor to demonstrate the potential for tailoring a microstructure in commercial spring steel that optimally balances mechanical properties, including yield strength, ultimate tensile strength, and ductility, without resorting to expensive alloying elements. This research is expected to provide pivotal insights and methodologies that can significantly impact the development of next-generation steels.

2 Material and Experimental Procedures

This study focused on commercial Mn-Si-Cr steel (Fe-0.65C-1.58Mn-1.05Si-0.41Cr, wt.%), aiming to design a Q&P processing route. Cylindrical specimens 4 mm in diameter and 10 mm in length were machined and prepared by electro-discharge machining (EDM). The samples were heat-treated using a Bähr DIL 805 A/D dilatometer to analyze the phase transformation behavior. Before carrying out the Q&P heat treatments, a preliminary quenching and tempering experiment was conducted to establish reference temperatures. Initially, the samples were heated to 900 °C at a rate of 15 °C/s to simulate the heating process and then quenched to room temperature at a rate of 80 °C/s. The quenched sample was then subjected to a tempering treatment, where it was heating to 500 °C at a rate of 15 °C/s to analyze the martensite lattice relaxation coupled with the decomposition of untransformed austenite as a function of temperature. Critical Q&P temperatures, A_{c1} , A_{c3} , M_s , and times were determined. The resulting microstructure was characterized by various techniques, including field-emission scanning electron microscopy (FE-SEM), X-ray diffraction (XRD), and electron backscattered diffraction (EBSD), to understand

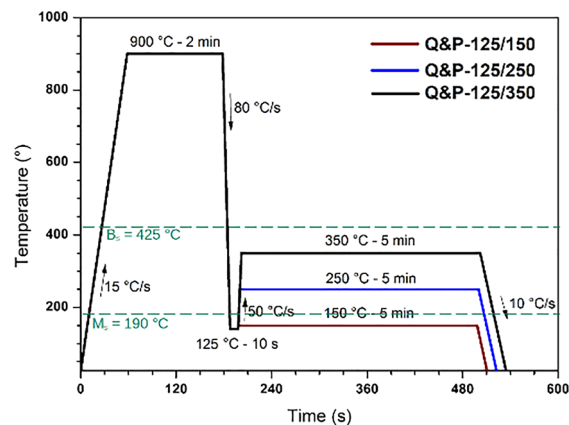


Fig. 1 Schematic of the proposed quenching and partitioning process, followed by bainitic transformation

the microstructural evolution. Finally, tensile tests were performed to verify the improvement of the tensile behavior of the modified microstructure compared to its original state.

Figure 1 illustrates the Q&P cycles implemented in this study. The obtained results were used to identify the nose temperatures and start times for the bainitic and martensitic transformations (B_s and M_s , respectively). Moreover, these results guided us in setting appropriate isothermal periods and cooling rates. This can help ensure the development of a homogeneous matrix microstructure, constituted primarily by martensite and lower bainite, while preventing the formation of coarse carbide/cementite and the emergence of freshly formed martensite at the end of the Q&P process.

To ensure clarity in our methodology and justification of the proposed complex heat treatments, we further elucidate the optimization process of the Q&P cycles in various sections of our paper. The heating/cooling rates, holding times, and tempering temperatures were optimized based on detailed investigations presented in the following sections: "3.2. Dilatometry and phase transformation temperatures," where the heating rate to austenitization and rapid quenching rates are explained; "3.3. Tempering kinetic of quenched sample," which discusses the kinetics of tempering and transformation processes; and "3.4. Dilatometry response during Q&P processing," where the partitioning stage timing is determined. These sections collectively provide a comprehensive understanding of our optimized Q&P process.

The microstructural evolution of all investigated specimens subjected to the proposed Q&P heat treatments was investigated by scanning electron and electron backscattered diffraction techniques. X-ray diffraction (XRD) analysis was also performed to determine the relative fractions of FCC—retained austenite (V_γ) and body-centered cubic—BCC—ferrite (martensite/bainite— V_α) phases. A field-emission scanning electron microscope (SEM-FEG-Inspect F50) was used to analyze the microstructure details

for both the as-received and Q&P-treated samples to quantitatively determine the distribution, size, morphology of the phases, and microconstituents in the microstructure. Metallographic samples were prepared by mechanical grinding using SiC paper of up to #1200 grit, followed by polishing with 6-, 3-, and 1- μm diamond paste. The microstructure was revealed by etching in 3% Nital for approximately 15 s. Microhardness was assessed using a Shimadzu (HMV-2TADW) microhardness tester, applying a load of 2.97 N (300 g—HV_{0.3}) for 15 s. The reported microhardness values represent averages from ten indentations.

X-ray diffraction analyses were conducted over a 2θ range of 35° to 120° with a step size of 0.025° and a scanning rate of $5^\circ/\text{min}$, operating at 40 V and 150 mA with Cu radiation ($\lambda = 0.15406 \text{ nm}$). The volume fraction of retained austenite was calculated based on the integrated intensity of the (111) γ , (200) γ , and (220) γ peaks of FCC-phase, as well as the (200) α and (211) α peaks of BCC phase [23]. The volume fraction of retained austenite was calculated using Eq. (1) [24]:

$$V_\gamma = \frac{1.4 \times I_\gamma}{1.4 \times I_\gamma + I_\alpha} \quad (1)$$

where V_γ , I_γ , and I_α are the volume fraction of retained austenite, the average integral intensity of (111) γ , (200) γ , and (220) γ FCC peaks, and the average integral intensity of (110) α , (200) α , and (211) α peaks [25]. The lattice parameter was then calculated using Eq. (2) based on {200} ferrite peak, where λ , {hkl}, and θ_{hkl} are the wavelength of radiation, the three Miller indices, and the Bragg angle, respectively.

$$a = \frac{\lambda \sqrt{h^2 + k^2 + l^2}}{2 \sin \theta_{\text{hkl}}} \quad (2)$$

The carbon concentration of retained austenite (X_c) was determined, in weight percent, using the austenite lattice parameter (a_γ), measured in Angstroms, from FCC {111} and {200} peaks, according to Eq. (3) [26]:

$$X_c = \frac{a_\gamma - 3.547}{0.046} \quad (3)$$

Dislocation density, micro-strain, and crystallite size were estimated from the XRD pattern using Debye–Scherer's equation [27] in conjunction with the Stokes and Wilson formula [15]. The defect density (δ) was evaluated using $\delta = \frac{1}{D^2}$. In this equation, D denotes the critical nucleus size; a parameter linked to the correlation between grain size and peak broadening per the Debye–Scherer's equation is [27, 28]: $D = \frac{k\lambda}{\beta \cos \theta}$. In this equation, k represents the shape factor equal to 0.9, λ is the X-ray wavelength, β refers to the full width at half maximum (FWHM), and θ is the X-ray

diffraction angle. Additionally, the micro-strain was calculated using the Stokes and Wilson equation [29]:

$$\varepsilon = \frac{\beta}{4 \tan \theta} \quad (4)$$

For medium carbon steel ($\approx 0.6 \text{ wt. \%}$), the c/a ratio can be determined as long as the (002) and (200) peaks of martensite are distinctly separated. The (200) martensite peak should be symmetrically aligned in BCC martensite, while the value of the c lattice parameter tends to exceed that of the a -lattice parameter in the BCT martensite structure. The Rietveld refinement was used to deconvolute overlapped martensite (002) and (200) peaks and thereby determine the c/a ratio of the martensite. In this respect, the martensite (002) peak was allocated on the left-hand tail and the martensite (200) peak on the right-hand tail, given the tetragonal ratio $c/a > 1$ [30–32].

The electron backscatter diffraction (EBSD) technique was employed to gather pertinent data for a comprehensive material characterization, including crystal orientation mapping, texture, grain size distribution, geometrically necessary dislocations (GND), grain boundary distribution, and kernel average misorientation (KAM). Furthermore, it was used to predict the local straining via the application of Schmid and Taylor factors. EBSD measurements were conducted using a FEI Inspect 50 FEG-SEM microscope, with an acceleration voltage of 20 keV, specimen tilt angle of 70° with a working distance between 15–30 mm, and a scan step size of approximately 0.1 μm . EBSD samples were prepared through conventional mechanical grinding and polishing, with a final polishing stage using a 0.05- μm oxide polishing suspension (OPS) for a duration of one hour. Lastly, the TSL OIM analysis 7 and A-TEX [33] tools were utilized for a detailed EBSD analysis, which facilitated the examination and modeling of crystallographic textures.

To provide direct evidence of the martensite matrix, the sample was examined using transmission electron microscopy (TEM). For TEM analysis, the sample was prepared using a focused ion beam (FIB) technique. The observations were conducted with a Thermo Fisher/FEI Titan Cubed Themis microscope, operating at 200 kV and equipped with an X-FEG electron source. Selected-area electron diffraction (SAED) analysis and indexation of diffraction electron spots were performed using the CrysT-Box—Crystallographic Tool Box software [34, 35].

In order to investigate the local mechanical performance of individual phases in the resultant multiphase steel, a nanoindentation test was conducted using a Triboindenter TI 950 (Hysitron Inc.), operating in load control mode. A matrix of 5×5 indentations was implemented, employing a maximum load of $10^4 \mu\text{N}$ with a Berkovich-type indenter. This process facilitated the gathering of elastic

and plastic properties derived from load–displacement (P–h) curves, calculated via nanoindentation. Tensile properties such as yield strength, tensile strength, elongation, yield ratio, work-hardening coefficient, and the modulus of toughness (or formability index) were characterized using sub-sized tensile specimens, extracted from dilatometry samples. Following the heat treatments, these dilatometry specimens were meticulously machined using an electron discharge machine (EDM) to fabricate sub-sized tensile specimens. These specimens conformed to the ASTM E8/E8M standard for sub-sized specimens, resulting in a flat dog-bone shape with a gage length of 4 mm, a gauge width of 2 mm, and a thickness of 1.5 mm, as justified in the references [24, 36]. Tensile testing was conducted on an Instron model 3369 servo-hydraulic testing machine at room temperature, employing a strain rate of $1.0 \times 10^{-3} \text{ s}^{-1}$. To ensure the reliability and reproducibility of our results, each sample underwent three separate tests, and the average values along with the standard deviation are presented in the manuscript. This approach allowed for a comprehensive analysis of the mechanical properties, ensuring that our findings are robust and representative of the material's behavior under tensile loading.

3 Results and Discussion

3.1 Characterization of the Original Microstructure

The as-received steel exhibited a fully pearlitic microstructure, as depicted in Fig. 2a, with an absence of carbide precipitates at the grain boundaries. Pearlite, which comprises soft ductile ferrite layers interspersed with hard, brittle, and cementite layers, provides exceptional work-hardening behavior. The dislocations in orthorhombic cementite possess limited mobility, while the crystallographic defects impede the glide of dislocations, particularly at the ferrite–cementite interfaces. As a result, a concentration of stress/strain in the interface area strengthens the steel. The pearlitic microstructure, characterized by ultrafine lamellar spacing and no inclusions, presents an estimated cementite lamellae thickness and interlamellar spacing of $70 \pm 25 \text{ nm}$ and $135 \pm 45 \text{ nm}$, respectively, as shown in Fig. 2b. The initial microhardness of the pearlitic structure was $355 \pm 25 \text{ HV}$, exhibiting the fine grain sizes and ultrafine interlamellar spacing typical of pearlitic structures [37, 38]. Notably, the pearlitic structure is widely used in industrial equipment due to its remarkable strength, wear resistance, fatigue resistance, and toughness. Coupled with its cost-effectiveness and ease of maintenance, these attributes make it an essential choice for such applications.

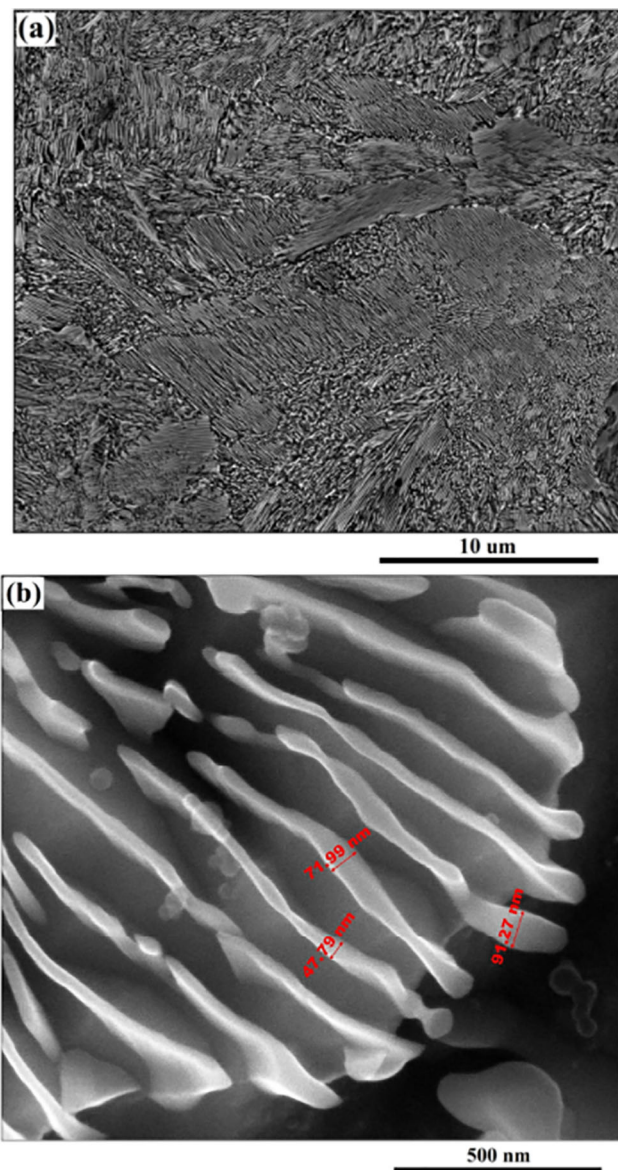


Fig. 2 a and b High-resolution SEM micrographs showing the as-received microstructure

3.2 Dilatometry and Phase Transformation Temperatures

The heat treatment parameters for the steel under investigation were established by heating the steel at a rate of 15 °C/s to 900 °C , followed by rapid quenching to 50 °C at a rate of 80 °C/s . The observed dilatation changes during continuous heating and cooling corresponded with the phase transformation from BCC ferrite to FCC austenite during heating stage and subsequently, the transformation from FCC to BCT under rapid cooling, as observed in Fig. 3.

The temperature for the start of austenitization (A_{c1}), the completion of austenitization (A_{c3}), and martensite start (M_s) were approximately $732 \pm 2 \text{ °C}$, $745 \pm 2 \text{ °C}$, and 190 ± 3

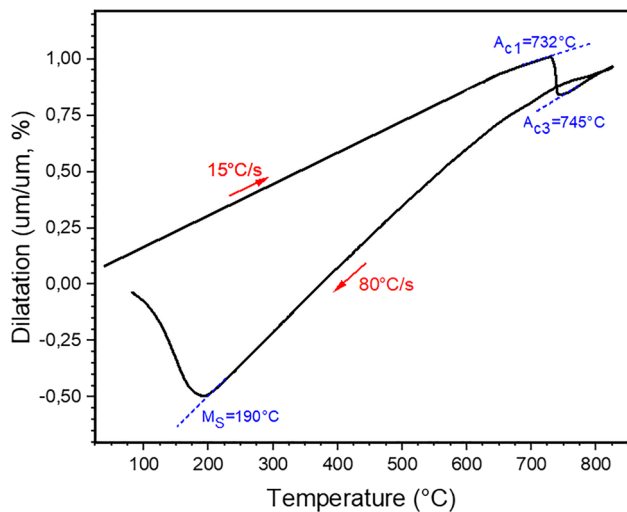


Fig. 3 Dilatation changes during heating and quenching stages

°C, respectively, as denoted by the dilation curve in Fig. 3. The quenching temperature, which controls the volumetric fraction of martensite and austenite, was determined through the Koistinen–Marburger relation [39] (Eq. 5), which is based on the level of supercooling relative to the M_s temperature.

$$V_\gamma = \exp\left(-1.10 \times 10^2 (M_s - T_q)\right); M_s > T_q > -80^\circ\text{C} \quad (5)$$

In this equation, V_γ refers to the volumetric fraction of retained austenite and T_q represents a specified temperature lower than M_s . Following a quenching process performed at 125 °C, the primary martensite (M1) constituted approximately $52 \pm 2\%$ of the microstructure of the steel, with the residual untransformed austenite accounting for about $48 \pm 2\%$. Notably, this untransformed austenite is rich in carbon and silicon content. Such a state is favorable for carbon to partition from the carbon-saturated martensite into the remaining austenite, thereby promoting further bainitic transformation and the precipitation of transition carbides.

3.3 Tempering Kinetic of Quenched Sample

The behavior of BCT martensite and the surrounding untransformed austenite was examined by conducting a tempering treatment at 500 °C with a heating rate of 15 °C/s, as depicted in Fig. 4. X-ray diffraction analysis revealed that the quenched sample comprised approximately 82 ± 2 vol.% pre-formed martensite and 18 ± 2 vol.% retained austenite. As the length change of the as-quenched martensite was recorded up to 500 °C, the results displayed four different regions: (i) the relaxation of the martensite lattice, (ii) the decomposition of untransformed austenite into bainite, (iii) the precipitation of transition carbides, and (iv) the cementite

coarsening [8, 31, 40, 41]. The critical value of stored energy, which determines the initiation of phase transformation, was determined via the first differentiation method. The precipitation of flaky transition-type ϵ -carbides during tempering at 200 °C in Q&P martensitic steel with medium carbon content was confirmed by Zhang et al. [41] using the selected area electron diffraction (SAED) patterns.

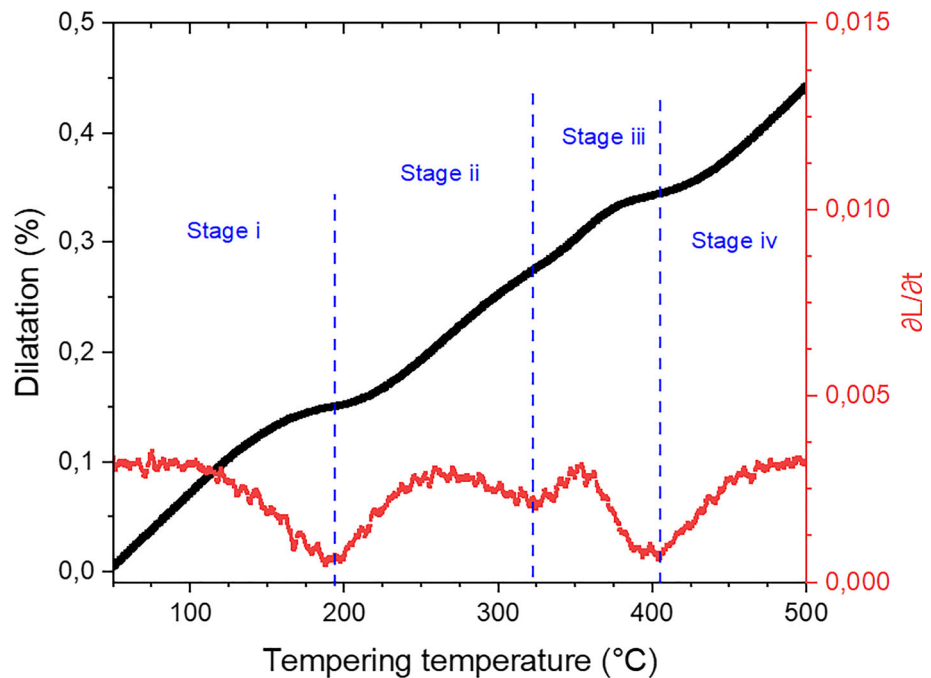
During tempering, the precipitation of transition carbides can cause net expansion of martensite and the isothermal decomposition of austenite into bainite, resulting in a gradual expansion between 225–325 °C. Transition carbides, such as HCP- ϵ epsilon, η -carbide, and Hägg carbide, can precipitate at low temperatures, ranging from 200–400 °C [42–44]. The formation of cementite during tempering is another important factor in microstructural evolution, where the formation of brittle coarse cementite can result in strong Mn concentration gradients between the cementite and BCC matrix, influencing subsequent bainitic transformation and austenite reversion mechanisms. Wu et al. [45] studied the kinetics of cementite coarsening during martensite tempering of medium carbon ternary Fe-C-Mn steels and determined that to prevent the formation of strong Mn concentration gradients and the resulting brittle cementite coarsening, the maximum partitioning step should occur at 350 °C for a duration of 5 min.

Cementite formation is influenced by various factors, including tempering temperature, alloying elements, and the kinetics of carbon diffusion. At higher tempering temperatures (around 400 °C to 600 °C), cementite is the predominant carbide phase formed [46]. Alloying elements like Si and Al can delay the transition from transition carbides (like ϵ -carbide or η -carbide) to cementite, particularly at lower tempering temperatures (200–400 °C) [45, 46]. The growth kinetics of cementite precipitates are also known to be faster at high-angle grain boundaries due to accelerated carbon diffusion [47]. Moreover, Mn content in the alloy significantly influences the cementite formation, as Mn tends to partition into cementite during the tempering process, affecting both the composition and size of cementite particles. This Mn enrichment in cementite and the resulting Mn concentration gradients in the matrix are critical in driving the coarsening reaction and influencing subsequent transformations in the steel microstructure. Understanding these mechanisms is vital for tailoring the tempering process to achieve desired microstructural features and properties in our steel.

3.4 Dilatometry Response During Q&P Processing

Figure 5a presents a detailed analysis of the normalized length changes in Q&P dilatometry specimens that were initially quenched to 125 °C before undergoing isothermal holding at 150 °C, 250 °C, and 350 °C for a period of 600 s. At 150 °C, there is a consistent decrease in length, a trend

Fig. 4 Dilatation curve (black line) and the first differentiation method ($\partial L/\partial t$, red line) under constant heating rate at 15 °C/s during the investigation of tempering of a fully quenched sample



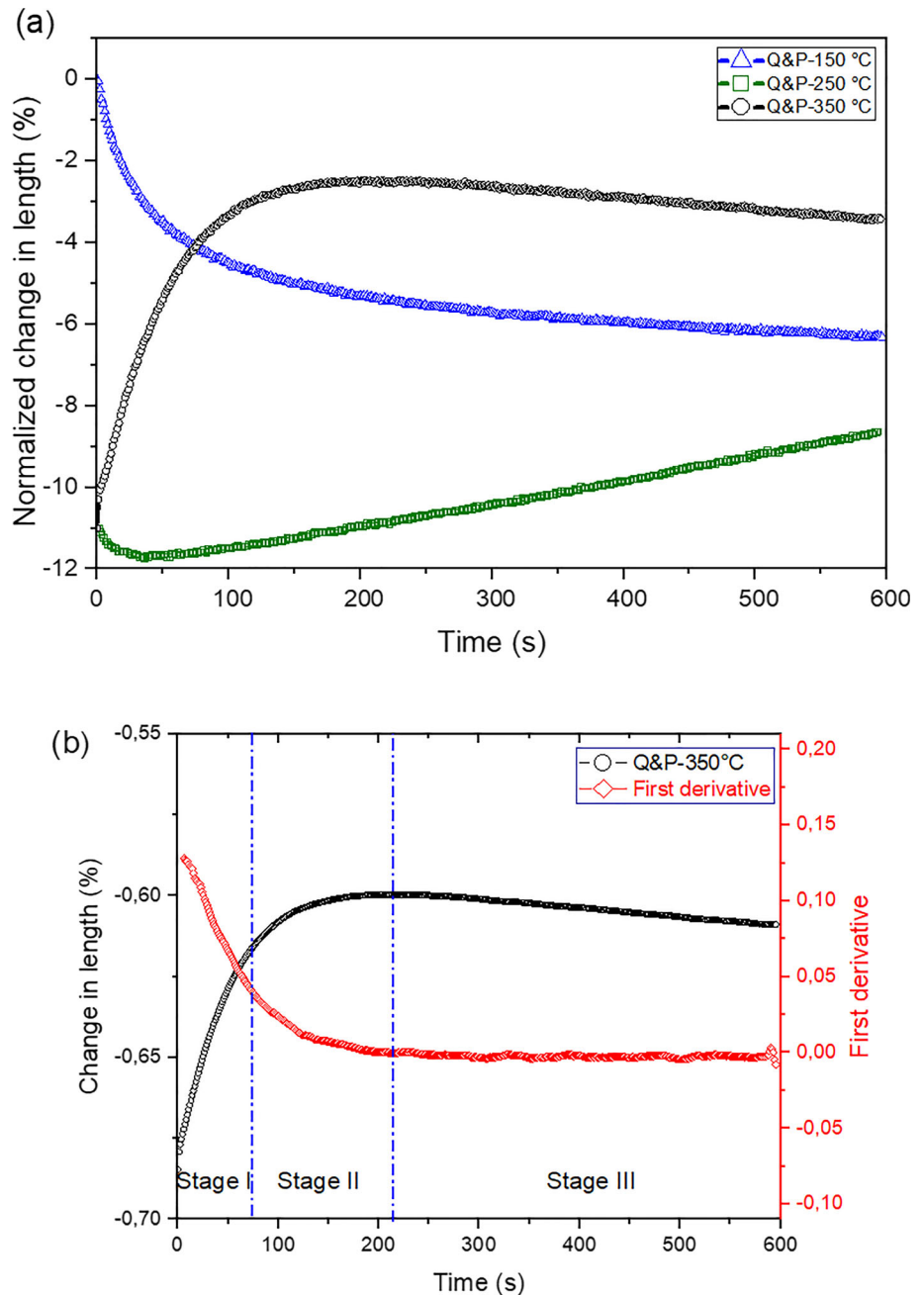
which can likely be attributed to the reduction of martensite tetragonality and the movement of carbon to dislocations and clusters. In the case of specimens held at 250 °C, a slight initial contraction at the onset of the isothermal treatment, followed by a sustained expansion throughout the remainder of the isothermal phase. This pattern could indicate the occurrence of carbon partitioning from the supersaturated martensite into the adjacent austenite, which would result in an increased carbon content within the remaining austenite. However, this should not preclude consideration of other possible mechanisms, such as the formation of isothermal martensite and bainite transformation, which might also contribute to the observed length changes. Considering that the degree of expansion attributed to carbon partitioning is typically minimal, the noticeable change displayed in Fig. 5a could be indicative of further microstructural transformations taking place. Figure 5b charts the length changes and the first derivative thereof ($\frac{d\Delta L}{dT}$) for the Q&P-125/350 sample during the isothermal hold at 350 °C over a span of 600 s. A significant expansion is seen within the first 100 s, which then transitions into a stabilization phase, ultimately culminating in a decrease in length. Further inquiry is warranted to comprehensively understand the processes leading to these dimensional alterations. Future investigations could leverage atom probe tomography, a tool that could prove highly instrumental in unveiling the underlying microstructural activities and confirming the existence of clusters or other features contributing to the dimensional changes observed.

The dilatometry analysis revealed three distinct stages, each exhibiting different behaviors. During stage I, a rapid volume expansion occurred within the initial 70 s, which can

be attributed to carbon partitioning from the carbon-enriched martensite to the adjacent untransformed austenite. This initial diffusional-based reaction correlates with an increased austenite lattice parameter, induced by the increased carbon concentration of dissolved carbon within this phase. In stage II, a stabilization in the length change is observed. Finally, stage III exhibits a tendency toward contraction, primarily associated with carbide precipitation within the acicular martensite and the decomposition of austenite into bainitic-ferrite and carbides. Previous literature suggests [48] that the presence of Si in the chemical composition, combined with a short-time of isothermal treatment, enhances the refinement of precipitated carbides and diminishes the volume fraction of martensite by boosting the stability of the retained austenite. The progressive increase in austenite stability is a consequence of carbon partitioning from martensite to the austenite. The formation of fine carbide precipitates impedes the creation of blocky retained austenite and favors the development of a more stable nanometric film-like Si-enriched retained austenite between the martensite laths. This phenomenon is consistent with findings reported in prior studies [48–50].

The observations made in Fig. 5 at 350 °C, particularly the initial rapid expansion followed by stabilization and subsequent contraction, can indeed be attributed to the diffusion of carbon. During the initial phase of isothermal holding at this temperature, the carbon-enriched martensite experiences carbon partitioning into the adjacent untransformed austenite. This diffusion of carbon results in an increased carbon concentration in the austenite phase, leading to an expansion in volume. As the process progresses, the austenite

Fig. 5 **a** Change in length observed in the dilatometry specimens during the isothermal holding at 150 °C, 250 °C, and 350 °C for 600 s, and **b** change in length and its first derivative ($\frac{d\Delta L}{dT}$) in the Q&P-125/350 sample during the isothermal stage



lattice parameter increases due to the higher carbon content, stabilizing the overall structure. The latter stages of contraction are likely a consequence of carbide precipitation within the martensite and the decomposition of austenite into bainitic-ferrite and carbides. The presence of Si in the alloy, as previously discussed in the literature, plays a significant role in this process by enhancing carbide refinement and promoting the stability of the retained austenite, which is further enriched with carbon as a result of this diffusional process.

This complex interplay of carbon diffusion and microstructural transformation at 350 °C is crucial for understanding the evolving properties of the material during the Q&P process.

3.5 X-ray Diffraction Analysis of Q&P Specimens

XRD analysis was performed on samples subjected to different Q&P processes and these were compared with the as-quenched sample. The XRD pattern for the as-quenched sample revealed typical ferrite peaks and minor retained austenite peaks. Samples treated with 150 °C and 250 °C

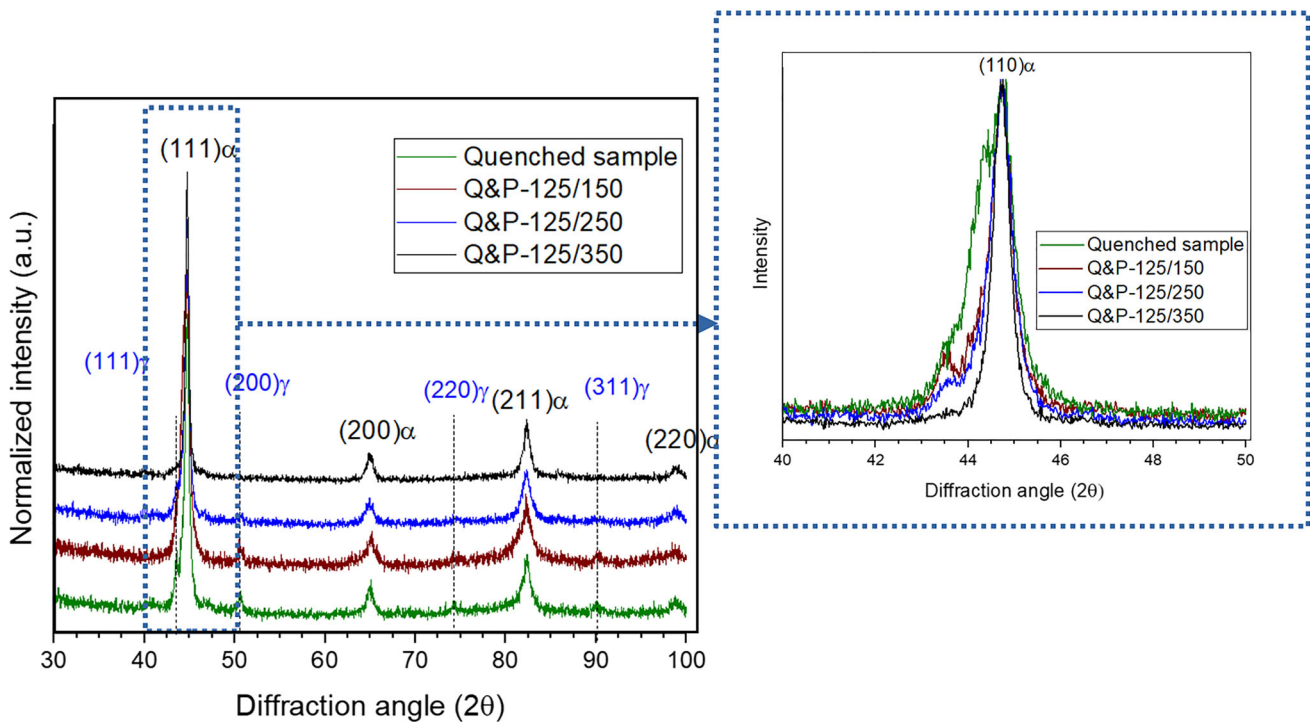


Fig. 6 XRD pattern obtained from investigated specimens

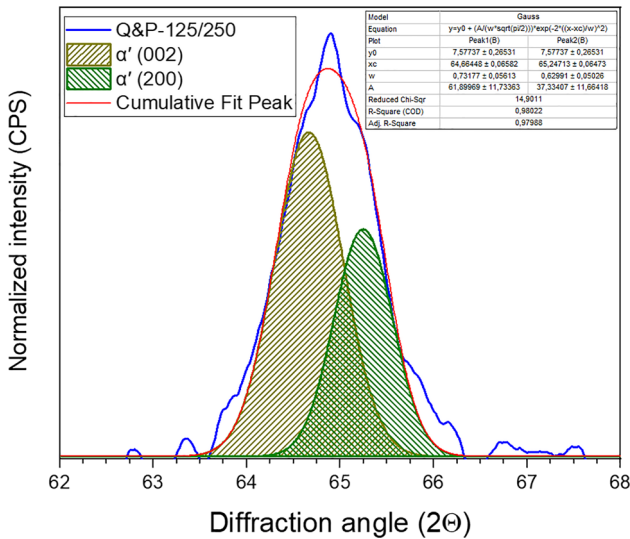


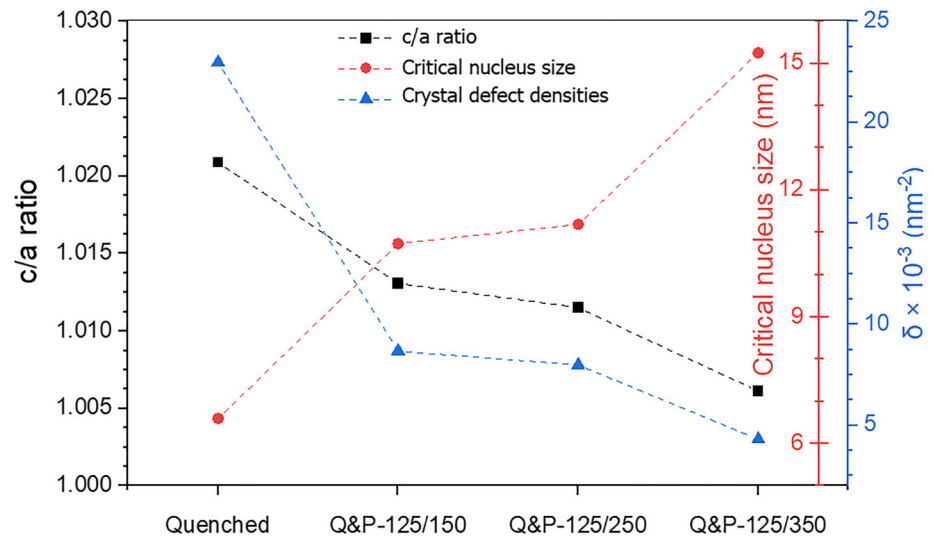
Fig. 7 (002) peak deconvolution of the Q&P-125/250 sample

Q&P processes also exhibited small austenite peaks, albeit less intensive. However, in the sample treated with 350 °C Q&P process, the austenite peaks were nearly indistinguishable. The volume fraction of retained austenite showed a consistent decrease from $18 \pm 2\%$ in the quenched sample to $11 \pm 1\%$, $4 \pm 1\%$, and $2 \pm 1\%$ for the Q&P-125/150, Q&P-125/250, and Q&P-125/350 samples, respectively. Simultaneously, the pronounced and wide $(111)\alpha$ peak observed in the as-quenched sample became narrower and shifted

rightward with increasing Q&P partitioning temperature, indicating a loss of carbon and tetragonality in martensite. The initial microstructure set the initial phase fraction and stability of the retained austenite. At the same time, subsequent partitioning parameters, such as temperatures and time, were the primary factors influencing the decrease in the volume fraction of austenite. It is noteworthy that the stability of austenite could be enhanced due to carbon enrichment [48]. For instance, based on the $\{111\}\gamma$ peak, the carbon concentration in the retained austenite for Q&P-125/250 sample was determined to be approximately 3.58 ± 0.5 wt.%. This increased concentration can be attributed to the diffusion of carbon atoms from the pre-formed martensite to the remaining austenite, which serves to stabilize the retained austenite [23, 51].

Dislocation densities were evaluated through the modified indirect Williamson–Hall method, as proposed by Dragomir et al. [52] using XRD (Figs. 6 and 8). Broadening of the diffraction peaks caused by high dislocation densities, as a result of martensitic transformation, can be measured by the full width at half maximum (FWHM, β) of these peaks. The modified Williamson–Hall method put forth by Alvarez et al. [53] accounted for anisotropic behavior induced by changes in the diffraction vector, incorporating the average contrast factor of dislocations. The sample heated to Q&P-125/150 displayed dislocation densities nearly five times greater than those observed in the as-received sample. This significant increase is due to the higher amount of martensite formed

Fig. 8 Variation of the c/a ratio, critical nucleus size, and defect densities of a quenched sample with treated specimens



under these conditions. However, an escalating partitioning temperature led to a gradual decrease in dislocation densities as the martensite lattice relaxed, carbon was redistributed, and residual austenite decomposed into carbide and ferritic-bainite. The Q&P-125/150 sample presented a substantial rise in both crystal defect densities and micro-strain, associated with a leftward peak shift and peak broadening, which could be related to lattice distortion occurring during the martensitic transformation under quenching. As expected, increasing the partitioning temperature resulted in a progressive decrease in crystallographic defects and micro-strain, attributable to relaxation of the martensite lattice, redistribution of carbon, and decomposition of the remaining austenite into carbide and ferritic-bainite.

It is well known that carbon content affects the tetragonality (c/a ratio) of martensite, with higher carbon content shifting the martensite phase transformation from BCC to body-centered tetragonal (BCT) [31, 54, 55]. The c/a ratio of martensite was calculated by deconvolution of overlapped (002) martensite peaks (i.e., α' (002) and α' (200)) and was found to decrease as the partitioning temperature increased. This suggests that carbon atoms are being partitioned from the athermal saturated martensite lath to lattice defects and the surrounding thin film austenite at the nanoscale [56]. This results in martensite lath carbon depletion and carbon enrichment in austenite during the partitioning process. The shift in the α' (002) and α' (200) martensite peaks to lower angles during partitioning due to carbon depletion and loss of tetragonality further confirms the carbon partitioning phenomenon, which is consistent with Morsdorf's atom probe tomography study [47, 57]. The deconvolution of the (002) peak in the Q&P-125/250 sample is demonstrated in Fig. 7.

High carbon athermal martensite contains a high density of crystallographic defects, such as dislocations or internal twins, due to the development of an internal substructure,

as formulated in the double-shear mechanism of martensite formation [58]. As a result, athermal martensite exhibits the highest defect densities compared to other phases. During the partitioning stage, interstitial elements like carbon diffuse from the athermal martensite to the interlath-retained austenite, resulting in increased stability. The carbon content directly influences the lattice parameter and the residual stresses in saturated martensite. However, incomplete carbon partitioning from martensite to austenite can occur due to carbide precipitation inside martensite laths and carbon atom segregation to dislocations, leading to a decrease in the c/a ratio and defect density in the BCT phases (Fig. 8).

3.6 Microstructural Evolution

The microstructure of various Q&P-treated samples is shown in Fig. 9, demonstrating the substantial influence of the quenching temperature on the resultant microstructural constituents. When quenched at 125 °C, approximately 50% of the prior austenite was transformed into tetragonal athermal martensite. The Q&P-125/150 sample features a matrix comprising a small amount of retained austenite ($11 \pm 1\%$) intertwined with α' martensite (tempered martensite) and freshly formed martensite (untempered martensite). The untempered martensite with high carbon ($> 0.6 \text{ wt.\%C}$) displays both plate-like and lath-like structures, characterized by high dislocation density and carbon concentration. Under SEM, this untempered martensite presents as a sequence of thin, elongated plates or laths with relatively smooth surfaces, intertwined with plate-like high carbon martensite.

In Fig. 9, SEM images show that the quenching temperature significantly impacts the microstructure of Q&P-treated samples. In the Q&P-125/150 sample, SEM imaging shows a complex morphology of tetragonal untempered martensite, interspersed with nanoparticles of retained austenite

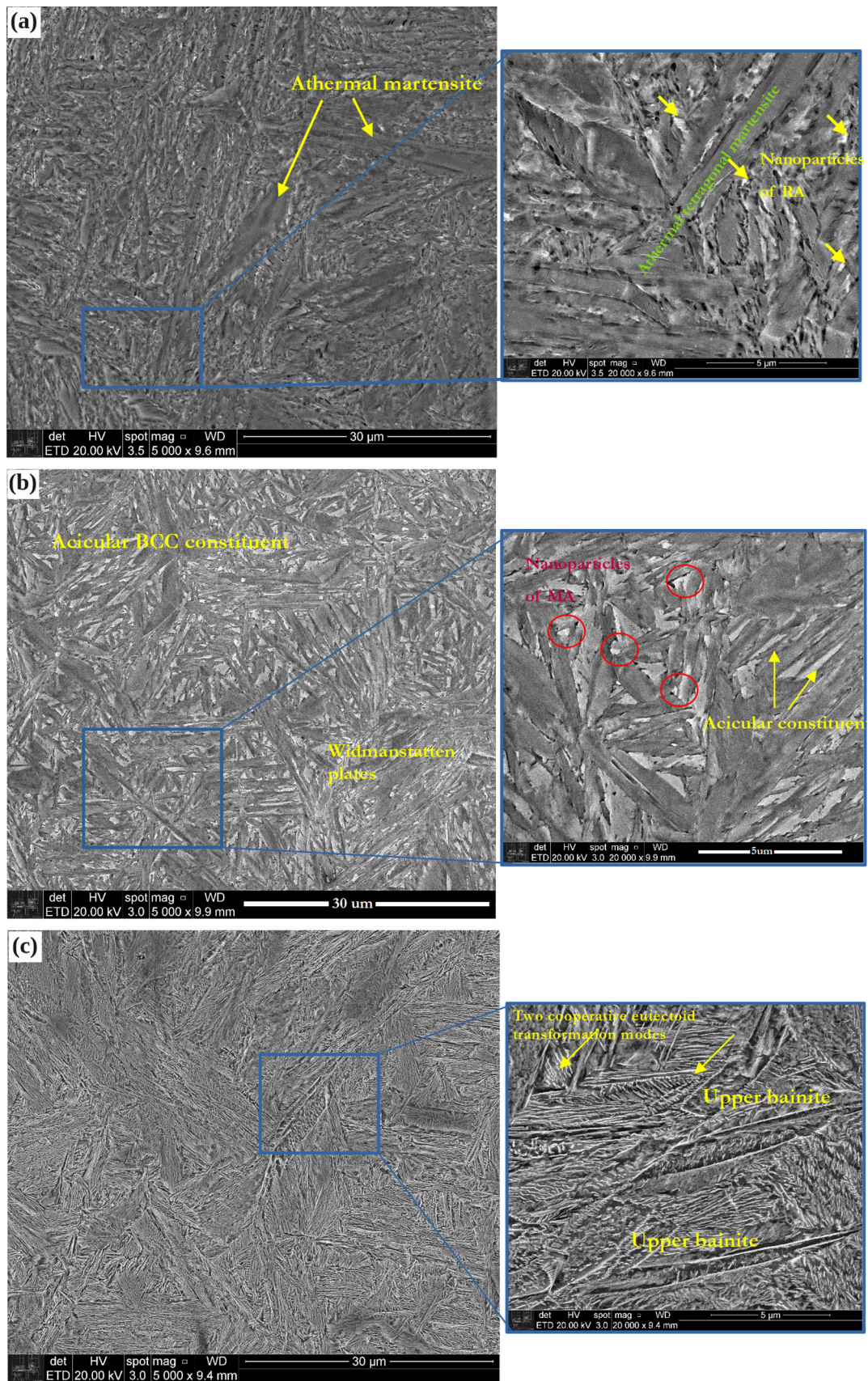


Fig. 9 SEM images of a Q&P-125/150, b Q&P-125/250, and c Q&P-125/350 specimens

precipitated between the martensite laths. Due to the fresh martensite formation during the cooling process, the hardness substantially increases to 780 ± 30 HV. When the partitioning temperature is increased to $250\text{ }^\circ\text{C}$, it triggers the formation of tempered martensite laths. This transformation primarily occurs due to the decomposition of supersaturated martensite, a process initiated by the diffusion of carbon atoms from the martensitic lattice. As a result, carbon precipitates from the martensite to form transition iron carbides (ϵ -carbide), which typically settle along dislocations and crystal defects within the martensite [54]. This process refines the microstructure, reducing internal stresses in the steel. Conversely, the relatively stable austenite (both chemically and mechanically) transforms into fresh martensite upon subsequent cooling. As a result, the Q&P-125/250 sample exhibited a multifaceted microstructure comprising tempered and freshly formed martensite, along with martensite/austenite (MA) microconstituents, yielding a hardness of 520 ± 20 HV. Additionally, approximately 4% of highly stable retained austenite was also observed, as shown in Fig. 9b.

At a partitioning temperature of $350\text{ }^\circ\text{C}$, as evident from Fig. 9c, the decomposition of martensite persistently progresses. During this phase, not only ϵ -carbide but also cementite (Fe_3C) begins to form. This phenomenon marks the second stage of partitioning, which encompasses the transformation of transition iron carbides into thermodynamically more stable cementite [55]. The formation of cementite is often associated with an increase in hardness due to its inherent properties. However, under certain conditions, cementite can be a part of a microstructural change that might lead to a different response in hardness. For instance, when cementite forms during martensite tempering, the overall hardness of the steel can diminish. Despite cementite being hard and brittle, its formation during tempering process can foster the softening of the steel. This phenomenon occurs as the martensitic structure transforms into a more ductile and tougher form, comprising both ferrite and cementite constituents. In the context of the elevated temperature mentioned, a larger fraction of retained austenite transforms into bainite. This transition is coupled with an augmented tendency for carbide precipitation within the residual austenite, potentially leading to its partial or even complete decomposition. It is important to note that in this scenario, the carbide precipitation is different from the formation of cementite during the tempering of martensite. Thus, the mechanisms responsible for alterations in hardness and ductility in this instance hinge on a complex interplay of phase transformations and precipitations.

Furthermore, it is important to consider the effect of martensitic transformation, which can cause stress/strain concentration fields in the hard-martensitic matrix, leading to

the initiation and propagation of microcracks [59]. Leveraging the TRIP effect can mitigate these issues, thereby enhancing the performance of engineering components subjected to great-magnitude external forces. When the partitioning temperature is raised to $350\text{ }^\circ\text{C}$, carbon partitioning intensifies, and the transformation coincides with decomposition of austenite into bainite, resulting in a low volume fraction (approximately 2%) of retained austenite, which is founded solely at the boundaries of martensite plates.

Gao et al. [60] proposed that the morphology of nanoscale retained austenite enhances the material's ductility and toughness by impeding fatigue cracks along the inter-plate martensite laths and prior austenite grain boundaries. As observed in the Q&P-125/350 sample, the hardness measure was optimized at 415 ± 20 HV due to the bainitic transformation. The variations in the fractions and morphologies of the retained austenite across the three conditions can be attributed to the austenite decomposition occurring during the isothermal stages, given that the initial treatment parameters remain identical. The addition of 1.05 silicon (wt.%) acts to impede cementite coarsening [61], thereby promoting the formation of uniformly distributed nanoscale cementite precipitates within the plates and inter-plates of martensite and bainite laths, leading to improved mechanical properties. No fresh martensite was detected in the Q&P-125/350 heat-treated sample, while tempered martensite contributes to mechanical strength and toughness. The nanoscale cementite boosts strength and ductility due to a precipitation-strengthening mechanism and a concurrent reduction in carbon content within the BCC matrix [62].

Figure 10 presents bright field TEM analyses combined with SAED images of Q&P-125/250 sample, illustrating a microstructure comprised of tempered martensite intermixed with bainite, each exhibiting distinct crystallographic planes. This intricate arrangement is a testament to the complex phase transformations induced by our specific heat treatment process. To elucidate the crystal orientation of the martensite plate observed in the bright field, SAED was conducted on the area highlighted by the red circle. The electron diffraction analysis reveals a zone axis of $[\bar{1}20]$, corresponding to a BCC crystal plane of $(2\ 1\ 2)$. This finding not only confirms the martensitic nature of the phase but also provides insight into the subtleties of its crystallographic orientation. The presence of these specific orientations and planes underscores the effectiveness of our Q&P process in tailoring the microstructural characteristics. These microstructural features play a pivotal role in defining the mechanical properties of the alloy, illustrating the intricate interplay between process conditions, microstructural evolution, and resultant material properties.

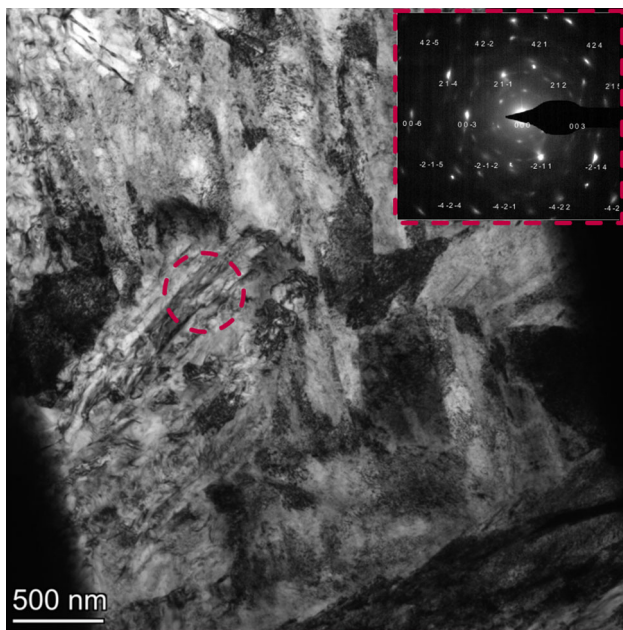


Fig. 10 presents bright field TEM analyses combined with SAED images of Q&P-125/250 sample

3.7 Crystallographic Orientation Evolution During Q&P Process

Orientation imaging microscopy (OIM) is a technique capable of offering intricate details about crystal and grain orientation, lattice distortion, and boundary characteristics in the final microstructure. With this method, maps such as the inverse pole figure (IPF), kernel average misorientation (KAM), and grain average image quality (IQ) can be generated. These analyses aid in estimating grain orientation, dislocation densities, and localized micro-strain within the microstructure. The size, orientation, and distribution of grains dispersed in the microstructure considerably affect the final mechanical and physical properties. The IPF map is particularly useful as it displays different colors corresponding to specific crystallographic orientations, making it easy to identify subgrain distributions and localized crystal orientation changes among the surrounding crystals, such as grains oriented along the (001) plane parallel to the rolling plane (RP), which are depicted in red.

In this study, the use of KAM maps proved crucial in interpreting the microstructural behavior of the material. These maps, generated by using the third neighboring point with an upper tolerance threshold of 5° misorientation, effectively minimized the impact of grain and subgrain boundaries. The color gradient distribution in KAM maps indicated that partitioning temperature inversely affected the KAM value, which decreased as the temperature increased. Martensite plates, which adopt one of the 24 possible orientation variants, contribute significantly to these observations. The martensite

plate displayed higher values relative to acicular martensite/bainite, a consequence of increased carbon content and lattice distortion. In contrast to the interior of the plate or lath, an intense strain field was identified around the boundaries. This strain stems from shear transformation and volume expansion during the subsequent bainitic transformations in the partitioning stage. While these transformations can trigger the formation of microcracks, they also hinder slip—a factor that warrants further investigation due to its potential implications on the mechanical behavior of the material.

For the Q&P-125/350 specimen, the BCC structure displayed a range of regions with low KAM values, suggesting that partial recovery and recrystallization processes have occurred, thereby alleviating the stored energy field. As a result, this sample is expected to exhibit more homogeneous ductility and be less prone to premature crack initiation. A synergistic analysis of KAM maps in conjunction with other significant maps, such as the IPF and IQ maps, enables the estimation of grain orientation, dislocation densities, and localized micro-strain in the microstructure, as shown in Fig. 11. This integrated approach provides new insights into the final mechanical and physical properties of the material, underscoring the potential of these techniques in furthering our understanding of material behavior.

In the Q&P-125/150 sample, as shown in Fig. 11, the supersaturated carbon martensite plate is distinctly identified through the highest values on the KAM and GND maps, a outcome of the maximum lattice distortion caused by tetragonality effects. Meanwhile, in the Q&P-125/250 sample, tempered martensite that exhibits less lattice distortion is evident. Furthermore, newly formed martensite, which occurred during the final quenching process, can be distinguished. The abundance of interfaces can be linked to the different crystallographic variations present within the martensite blocks. Lastly, the KAM map of the Q&P-125/350 sample exhibits the lowest internal energy, attributable to the annihilation of dislocations, the tempering of martensite, and the development of bainitic sheaves. Although the GND was significantly reduced compared to the other samples, stress concentrations were still noticeable within certain tempered martensite laths.

Figure 12 presents a composite image integrating the confidence index and band contrast for the Q&P-125/350 sample, which is characterized by tempered martensite within a bainite BCC matrix. This image notably highlights the fluctuating quality of band contrast across a specific martensite lath. The difference in band contrast quality is predominantly evident at the interface of the lath martensite, where elevated level of lattice distortion degrades the quality of band contrast. However, as the c/a ratio progressively diminishes across the martensite lath, this quality significantly improves. This enhancement indicates that lattice distortion, influenced by the c/a ratio, is crucial in determining the band contrast

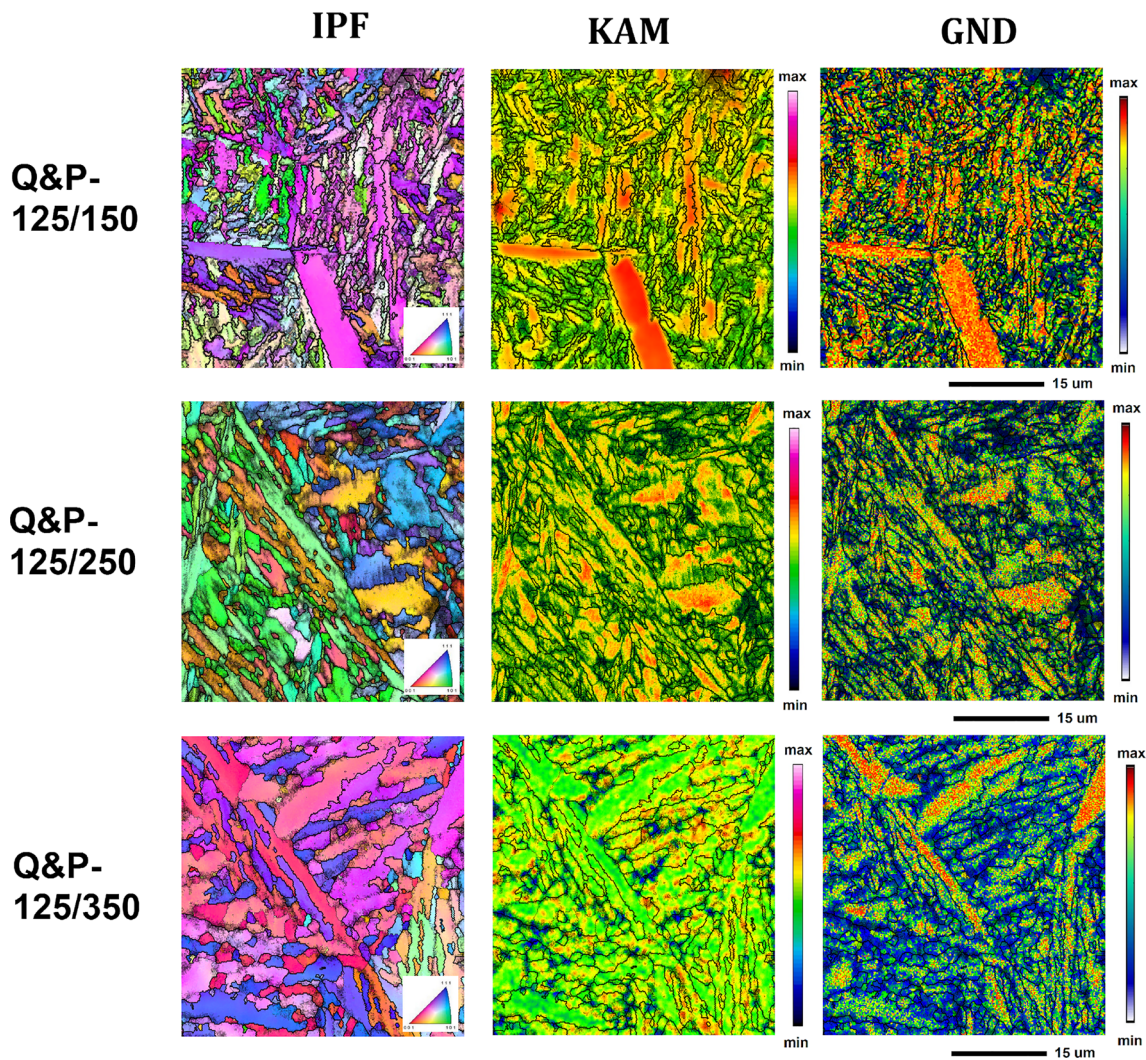


Fig. 11 EBSD analyses of normal direction IPF, KAM, and GND maps of the investigated specimens

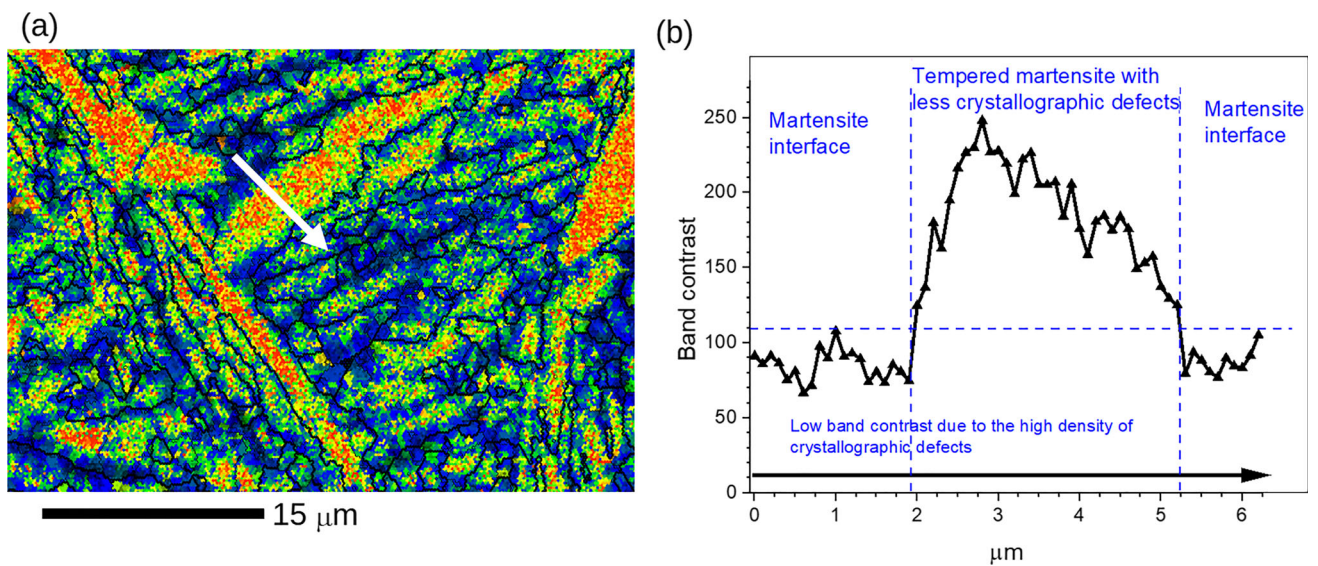


Fig. 12 a Band contrast and confidence index of the Q&P-125/350 sample and b the sectional profile of the labeled line (white arrow)

quality. It is well established that the tetragonality of martensite is a consequence of the unequal distribution of carbon atoms in the octahedral interstices of the BCC structure, leading to a change in the lattice parameter [55]. Furthermore, the state of the tetragonality of the martensite, dictated by the c/a ratio, also affects the phase transformation process. Therefore, understanding this tetragonality and its influence on lattice distortion is essential for a comprehensive interpretation of the observed confidence indexing and band contrast variations.

Though traditional EBSD methods struggle to detect localized lattice distortions, they can effectively analyze the resultant effects and dislocations. This allows the calculation of GND density, thus providing valuable insights into material behavior and evolution [63]. This approach first uses the KAM method to estimate the local misorientation level, then compares the variation of the misorientation angle of individual grains to calculate dislocation density and relate it to the crystal defect accumulations. Read and Shockley [64] proposed that the dislocation density between two distinct points could be estimated by $\rho_{GND} = \frac{\kappa \Delta\theta}{(b \Delta s)}$, where θ represents the misorientation angle, b is the magnitude of the Burgers vector, and s is the step size. The GND induced by edge dislocations primarily cause tilt rotations of the crystal lattice and their density can be estimated by accumulating the distortions to accommodate a given crystal misorientation. Based on a 200-nm step size, the average dislocation densities were estimated as 6.8×10^{13} , 2.3×10^{13} , and $7.4 \times 10^{12} \text{ m}^{-2}$ for the Q&P-125/150, Q&P-125/250, and Q&P-125/350 specimens, respectively. The promising mechanical resistance and ductility observed in the tempered martensite and bainite, generated through partitioning at 350 °C, can be attributed to a combination of factors, including the distribution of carbon atoms within the martensite structures, the influence of dislocations, and the inherent stresses. Our examination of the martensite and bainite boundaries unveils a landscape rich in carbon content, exhibiting a high degree of lattice distortion, which ensnares stress-induced dislocations. These concentrated stress nodes act as barriers to crack propagation, significantly enhancing fracture toughness, particularly evident in the Q&P-125/350 sample. These findings are consistent with the study of Gaudez et al. [65], which revealed that a significant proportion of carbon atoms migrate during the partitioning process. Recognizing the established theory of carbon partitioning—from supersaturated martensite to untransformed austenite—is crucial and widely accepted. In particular, carbon can diffuse quickly from supersaturated martensite to the martensite–austenite interface. Yet, Gaudez et al. [65] proposed an interesting phenomenon where not all carbon atoms in residual austenite migrate to form transition carbides, leaving the martensite still supersaturated with carbon. Other mechanisms may contribute to retaining carbon within the martensite. The transformation from austenite

to martensite is a diffusionless process that occurs rapidly, providing little time for atoms to diffuse. The volumetric changes associated with this transformation can generate stresses, potentially impeding the complete diffusion of carbon from martensite. Additionally, it is well established that dislocations can act as trapping sites for carbon atoms. The density of these dislocations increases during the formation of bainitic-ferrite laths, and given the lower degree of recovery in martensite compared to bainite, these dislocations can persist, facilitating carbon trapping. Carbide formation is not restricted to austenite or martensite—it can occur in both phases. The formation of carbides within martensite or austenite results from the precipitation of carbon atoms. In the context of this study, it is essential to differentiate between carbon migration to transition carbides and the conventional understanding of carbon partitioning and carbide formation in both phases.

Figure 13a presents the point-to-point misorientation of each specimen. The quenched and partitioned structures at 150 °C display a higher proportion of high-angle boundaries (HABs)—those with misorientation exceeding 15° between two adjacent pixels. However, as the partitioning temperature escalates up to 350 °C, the proportion of low and medium angle boundaries (LABs and MABs)—those with a misorientation less than 5° and within the range of 5° to 15°—also increases. The presence of silicon inhibits the rapid nucleation and coarsening of carbide particles, which in turn leads to the formation of nanoscale carbide precipitates inside the bainitic sheaves and acicular martensite, resulting in the generation of a high lattice disorientation. This significantly enhances the mechanical properties without compromising ductility. The BCC packet boundary and block boundary primarily consist of HABs with a point-to-point misorientation of approximately 60°. Consequently, the Q&P-125/350 heat-treated specimens are expected to exhibit more uniform plasticity due to a significant reduction in stored energy. Figure 13 also illustrates that the prevalent bainite and martensite structures exhibit the highest frequency at larger misorientation angles, primarily due to their distinct transformation mechanisms and microstructural features. These structures are formed during phase transitions in steel, with martensite evolving via a swift diffusionless transformation, and bainite forming through a displacive transformation at elevated temperatures. The rapid transformation of martensite from austenite provokes severe lattice distortion, giving rise to substantial internal stresses. These stresses, combined with the deformation stemming from this transformation, give rise to pronounced misorientation angles. Additionally, both martensite and bainite display high dislocation densities owing to their formation process. The accumulation of these dislocations can prompt the development of subgrain structures within individual grains, thereby amplifying misorientation angles. In the case of martensite, the occurrence

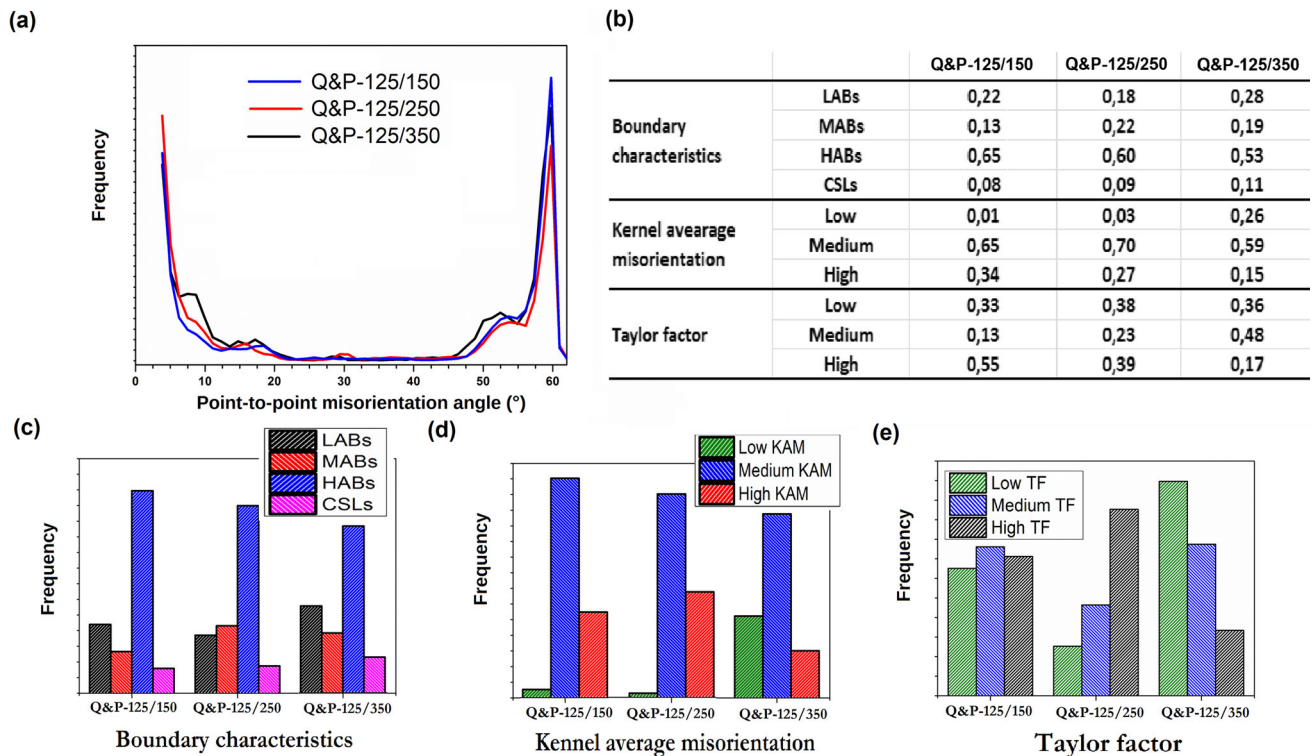


Fig. 13 a and b Point-to-point misorientation, c grain boundary characteristics, d Kernel average misorientation, and e Taylor factor charts of the investigated specimens

of mechanical twinning, a form of shear strain deformation, can also contribute to elevated misorientation angles. For bainite, the transformation process from austenite frequently involves carbide precipitation, which can further enhance misorientation angles. Ultimately, the distinctive transformation pathways and microstructural characteristics of these structures explain their propensity toward greater misorientation angles.

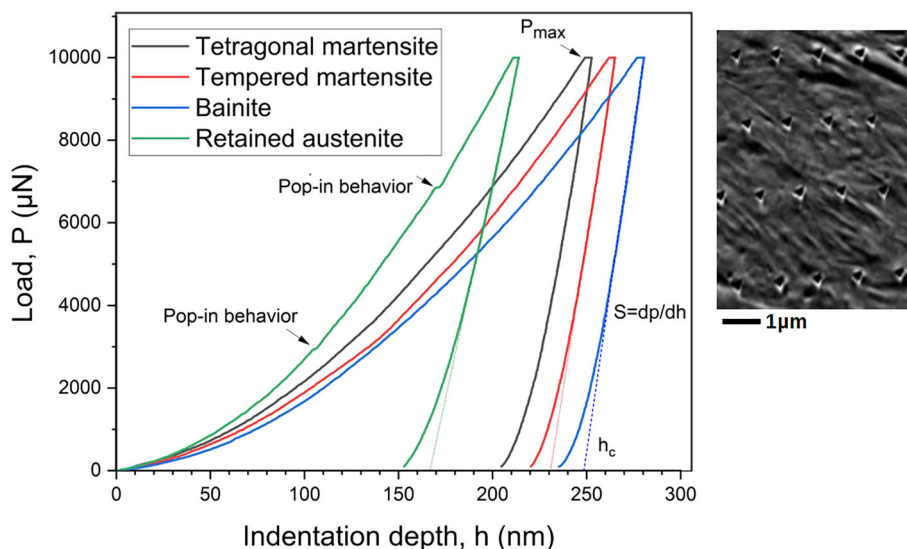
Li et al. [66] proposed a subdivision of packets into blocks which, despite sharing similar directions, exhibit different spatial orientations. These blocks can be further divided into sub-blocks. The KAM analysis presented in Fig. 13d demonstrates that the Q&P-125/150 sample had the highest level of stored energy due to the pure martensitic transformation. The partitioning temperature influenced the stored energy, causing stress relief and facilitating carbon partitioning from the supersaturated martensite into the untransformed austenite, followed by austenite decomposition into ferritic-bainite and nanoscale carbide. The Taylor factor maps analysis, shown in Fig. 13e, revealed that neighboring grains restrict plastic deformation of each grain. Soft grains, characterized by low Taylor factor values, are already oriented along activated slip systems. In contrast, grains with a medium Taylor factor can rotate and reorient to afford at least five independent slip systems for slipping. High Taylor factor grains, surrounded by

grains that prevent desirable reorientation, are more susceptible to intergranular and transgranular fracture phenomena. Therefore, the Q&P-125/350 process can yield the highest number of soft grains with low Taylor factor values, resulting in a good combination of strength and ductility.

3.8 Local Mechanical Properties Using Nanoindentation Test

The local mechanical properties of the multiphase structure resulting from the Q&P-125/350 treatment were analyzed using a 5×5 nanoindentation matrix. The analysis identified four distinct local mechanical properties: (i) retained austenite, represented by the green line, (ii) bainite microconstituent, represented by the blue line, (iii) higher mechanical resistance constituents such as tempered martensite, represented by the red line; and (iv) the hardest phase constituent, tetragonal martensite, represented by the black line. Load-indentation depth curves of nanoindentations for each constituent phase of the Q&P-125/350 treated sample are shown in Fig. 14. Importantly, pop-in behavior was detected in the retained austenite during the loading phase, which signifies the onset of the TRIP (transformation induced plasticity) phenomenon, leading to the creation of highly distorted and supersaturated martensite. Notably, indentations on grain or inter-phase boundaries were disregarded in the analysis.

Fig. 14 Load-Indentation Depth Curves for Q&P-125/350 Sample, includes nanoindentation profiles of each constituent phase and associated micrographs showing indenter locations



The tetragonal martensite showed the highest nanohardness value (6.38 ± 0.20 GPa) at a minor indentation depth of approximately 228.71 ± 0.05 nm. The nanohardness values for tempered martensite and bainite were 5.78 ± 0.18 GPa and 5.09 ± 0.32 GPa, respectively, with the greatest indentation depth (258.88 ± 0.05 nm) observed in the apparent bainite phase. Compared to the extremely low carbon content bainitic phase, tetragonal and tempered martensite displayed approximately 25% and 11% higher resistance, respectively. Bainite formation involves the diffusional phase transformation of retained austenite into extremely low carbon content ferritic-bainite with minimal internal energy. During partitioning, carbon is migrated out from the saturated martensite laths and is surrounded by retained austenite, thereby reducing the distorted energy associated with the displacive martensitic transformation. In contrast, tetragonal martensite, enriched with a high concentration of carbon atoms and exhibiting a high c/a ratio, showcased the highest nanohardness value, attributable to the local hardening induced by the geometrically necessary dislocations.

3.9 Effect of Multicomponent Microstructure on Tensile Properties

Figure 15 displays the engineering stress–strain curves of the investigated specimens, as well as microhardness values and tensile data provided in Table 1. The original as-received pearlitic structure exhibited a yield strength of 870 ± 10 MPa, an ultimate tensile strength of 1275 ± 15 MPa, and an elongation of approximately 14%. The Q&P-125/150 sample demonstrated a significant increase in both yield and tensile strength, but a notable reduction in ductility due to the formation of newly formed martensite, leading to a brittle structure with excessive elastic stored energy that promotes

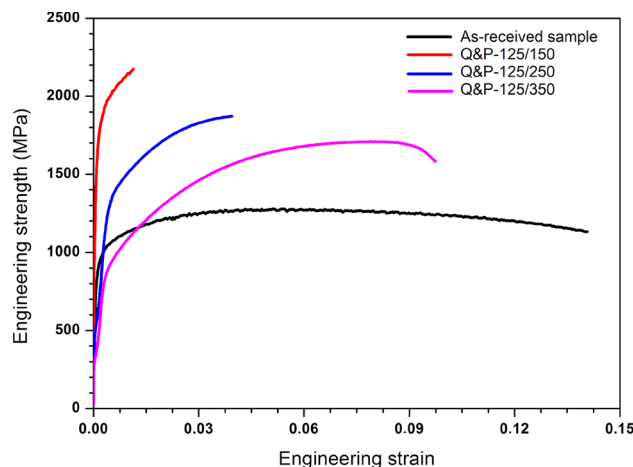


Fig. 15 Engineering stress–strain curves of investigated specimens

microcrack nucleation. Despite having the highest fraction of retained austenite, the Q&P-125/150 sample showed the lowest total elongation due to insufficient carbon partitioning. The Q&P-125/250 heat-treated sample also displayed high strength, with a yield strength of 1250 ± 15 MPa and ultimate tensile strength of 1870 ± 15 MPa; however, compared to the Q&P-125/150 sample, martensitic lattice relaxation and partial carbon partitioning reduced the total strength, while quadrupling the total elongation due to the presence of tempered martensite. Finally, the Q&P-125/350 sample presented a yield strength of 950 ± 15 MPa, an ultimate tensile strength of 1710 ± 15 MPa, and an elongation of approximately 9.7%. This balance between strength and ductility was achieved thanks to the tailoring of a complex, desirable microstructure, involving a fine dispersion of nanoscale carbide particles within the ferritic-bainite laths in low tetragonality tempered martensite. The sizable gap between the

Table 1 Microhardness and tensile data results of the investigated specimens

Sample	Hardness (HV _{0.3})	Yield stress (MPa)	Ultimate tensile strength (MPa)	Total elongation	Toughness* (kJ/m ²)
As-received	355 ± 25	870 ± 10	1275 ± 15	0.140 ± 0.005	85.50
Q&P-125/150	780 ± 30	1800 ± 15	2170 ± 15	0.011 ± 0.005	23.45
Q&P-125/250	520 ± 20	1250 ± 15	1870 ± 15	0.040 ± 0.005	68.65
Q&P-125/350	415 ± 20	950 ± 15	1710 ± 15	0.097 ± 0.005	118.59

*Toughness calculated from the area under the strain–stress curves

yield stress and the ultimate stress can be particularly beneficial for the processing coiled springs, which rely on cold forming of the pre-heat-treated material.

Typically, AISI 9260 steel exhibits a range of mechanical properties, with hardness between 321–375 HV, yield stress spanning 690–1200 MPa, and ultimate tensile strength ranging from 925–1860 MPa, coupled with an elongation of about 5–6% [12, 16, 17, 67]. These properties are generally associated with a microstructure dominated by tempered martensite, interspersed with cementite throughout. The presence of cementite, especially at grain boundaries or martensite interfaces, can create stress concentration sites, leading to potential crack initiation and propagation. In contrast, our Q&P-125/350 sample exhibits a remarkable combination of mechanical properties: a yield strength of 950 ± 15 MPa, an ultimate tensile strength of 1710 ± 15 MPa, and an elongation of approximately 9.7%, with a hardness of 415 ± 20 HV. This enhancement is attributed to a unique microstructure comprising approximately 50% tempered martensite and 50% ferritic-bainite, interspersed with ultrafine transition carbides. This novel microstructure, a result of the Q&P process, not only improves the hardness and strength but also significantly enhances ductility compared to typical AISI 9260 steels. The distribution of ultrafine carbides, as opposed to the coarser cementite typically found in AISI 9260, reduces the likelihood of stress concentrations and crack propagation. This innovative microstructural engineering through the Q&P process illustrates the potential for tailoring mechanical properties beyond the conventional capabilities of AISI 9260 steel, opening new avenues in material design and application.

The influence of the partitioning step, which involves carbon partitioning and bainitic transformation, on the mechanical properties and hardness of steels is well established. By controlling the phase constituents, it has been demonstrated that the ultimate tensile strength of commercial eutectoid steel (fine pearlite) can be increased from 1275 to 1710 MPa, signifying a 45% improvement. Nonetheless, this is accompanied by a decrease in ductility of 28% compared to the original pearlitic structure, even while achieving an impressive 38% enhancement in the energy absorbed at

fracture. The correlation between strength and ductility can be attributed to the dispersion of nanoscale carbide particles within the tempered martensite and ferritic-bainite needles, which evolve through the tailored Q&P process. Increasing the partitioning temperatures leads to greater degree of carbon partitioning from martensite, which in turn increases the stability of the residual austenite. This prompts the formation of nanoscale carbide particles, yielding significantly higher mechanical properties with only a slight loss in ductility. However, achieving high strength with good ductility in commercial eutectoid steel, which is a complex system composed of multiple structures and phases, remains a significant challenge due to the enormous combination of alloying elements and further thermomechanical processing. This study demonstrates the feasibility of achieving desirable material properties without resorting to expensive alloying elements. Instead, we manipulate the carbon depletion in the martensite matrix, reducing tetragonality. This is achieved by carefully controlling the partitioning stage, encompassing both temperature and time variables, to manage the bainitic transformation. Simultaneously, this approach circumvents the unwanted coarsening of cementite, further enhancing the optimization of the material's characteristics.

4 Conclusions

A novel quenching and partitioning (Q&P) heat treatment process was used to achieve a unique combination of strength and ductility in a commercial spring Mn-Si-Cr steel. This pioneering approach produced microstructural features and crystal boundary conditions that resulted in a desirable multi-phase microstructure and crystallographic lattice distortion. The main findings of this investigation can be summarized as follows:

Adjusting the partitioning temperature and time crucially controls lattice distortion in martensitic transformation, affecting internal stress and the martensite's tetragonality. Dilatometry reveals subtle phase transformations via volume changes. Combined with SEM and EBSD, it elucidates

microstructural evolution, including ferrite and bainite transformations.

Higher partitioning temperatures facilitate reduced lattice distortion and dislocation densities, resulting in a multiphase microstructure with nanoscale carbide particles in tempered martensite and ferritic-bainitic laths.

The inclusion of 1.05 wt.% silicon significantly suppresses cementite coarsening, promoting finer cementite dispersion in martensite and bainite phases.

The Q&P-125/350 sample exemplifies the ability to engineer desired microstructures in commercial spring steel without expensive alloying, achieving high yield strength (950 ± 15 MPa), ultimate tensile strength (1710 ± 15 MPa), and notable elongation ($\sim 9.7\%$).

Acknowledgements The authors would like to acknowledge the support given by the National Council for Scientific and Technological Development (CNPq, No. 304157/2020-1) and São Paulo Research Foundation (FAPESP, No. 2021/02926-4), Key Program of the Brazil Academy of Sciences. We also gratefully acknowledge the Brazilian Nanotechnology National Laboratory (LNNano) for their invaluable assistance in analyzing TEM samples for our study, conducted under the proposal ID 20230098.

Author contributions MM and EAAE planned the research, designed the experiments, and drafted the manuscript. DMAC helped in revising the manuscript and discussed the results. All authors contributed to and reviewed the manuscript.

Funding Open Access funding provided by Colombia Consortium. National Council for Scientific and Technological Development, 304157/2020-1, Mohammad Masoumi, São Paulo Research Foundation, 2021/02926-4, Mohammad Masoumi

Declarations

Conflict of interest The authors declare that they have no known competing financial interests or personal relationships that could have appeared to influence the work reported in this paper.

Open Access This article is licensed under a Creative Commons Attribution 4.0 International License, which permits use, sharing, adaptation, distribution and reproduction in any medium or format, as long as you give appropriate credit to the original author(s) and the source, provide a link to the Creative Commons licence, and indicate if changes were made. The images or other third party material in this article are included in the article's Creative Commons licence, unless indicated otherwise in a credit line to the material. If material is not included in the article's Creative Commons licence and your intended use is not permitted by statutory regulation or exceeds the permitted use, you will need to obtain permission directly from the copyright holder. To view a copy of this licence, visit <http://creativecommons.org/licenses/by/4.0/>.

References

- Park, J.; Min, K.M.; Kim, H.; Hong, S.H.; Lee, M.G.: Integrated computational materials engineering for advanced automotive technology: with focus on life cycle of automotive body structure. *Adv. Mater. Technol.* **2201057**, 1 (2022). <https://doi.org/10.1002/admt.202201057>
- Bleck, W.; Brühl, F.; Ma, Y.; Sasse, C.: Materials and processes for the third-generation advanced high-strength steels. *BHM Berg-Huettenmaenn. Monatsh.* **164**(11), 466 (2019)
- Zhao, Y.; Gao, Y.; Chen, D.; Chen, W.; Liu, J.; Liu, Z.: Enhancing strength and plasticity synergy in transformation-induced plasticity-aided lean duplex stainless steel based on the ultrafine-grained austenite. *J. Mater. Eng. Perform.* **31**(3), 2487 (2022)
- Zhang, B.; Zhao, M.M.; Dong, Y.; Misra, R.D.K.; Du, Y.; Wu, H.Y.; Du, L.X.: On the structure-property relationship in a novel 1000 MPa hot-rolled TRIP steel with strain-assisted ferrite transformation. *Mater. Sci. Eng. A* **821**, 141594 (2021)
- Wang, Y.; Xu, Y.; Zhang, T.; Li, J.; Hou, X.; Sun, W.: Effects of quenching temperature on bainite transformation, retained austenite and mechanical properties of hot-galvanized Q&P steel. *Mater. Sci. Eng. A* **822**, 141643 (2021)
- Dhara, S.; van Bohemen, S.M.C.; Santofimia, M.J.: Isothermal decomposition of austenite in presence of martensite in advanced high strength steels: a review. *Mater. Today Commun.* **33**, 104567 (2022)
- Skolek, E.; Szwejkowska, K.; Chmielarz, K.; Świątnicki, W.A.; Mysza, D.; Wiczorek, A.N.: The microstructure of cast steel subjected to austempering and B-Q&P heat treatment. *Metal. Mater. Trans. A* **53**(7), 2544–2560 (2022)
- Pashangeh, S.; Somani, M.C.; Ghasemi-Banadkouki, S.S.; Karimi-Zarchi, H.R.; Kaikkonen, P.; Porter, D.A.: On the decomposition of austenite in a high-silicon medium-carbon steel during quenching and isothermal holding above and below the Ms temperature. *Mater. Charact.* **162**, 110224 (2020). <https://doi.org/10.1016/j.matchar.2020.110224>
- Masoumi, M.; Echeverri, E.A.A.; Tschiptschin, A.P.; Goldenstein, H.: Improvement of wear resistance in a pearlitic rail steel via quenching and partitioning processing. *Sci. Rep.* **9**(1), 7454 (2019)
- Dalwatkar, R.; Prabhu, N.; Singh, R.K.P.: Effect of austempering temperature and time on mechanical properties of SAE 9260 steel. *AIP Conf. Proc.* **1957**(1), 40001 (2018)
- Yan, S.; Wang, Q.; Chen, X.; Zhang, C.; Cui, G.: Failure analysis of an automobile coil spring in high-stress state. *J. Fail. Anal. Prev.* **19**(2), 361 (2019)
- Hasanlou, S.; Vaseghi, M.; Samezadeh, M.: Modeling and experimental investigation of fracture behavior of hot-rolled hyper-eutectoid Si-Mn TRIP steel: heat-treatment effect. *Met. Mater. Int.* **28**(6), 1349 (2022). <https://doi.org/10.1016/j.matchar.2023.113523>
- Masoumi, M.; Ariza, E.A.; Centeno, D.; Tressia, G.; Márquez-Rossy, A.; Poplawsky, J.D.; Tschiptschin, A.P.: Achieving superior mechanical properties: Tailoring multicomponent microstructure in AISI 9254 spring steel through a two-stage Q&P process and nanoscale carbide integration. *Mater. Charact.* **207**, 113523 (2024)
- Mohtadi-Bonab, M.A.; Ariza, E.A.; Loureiro, R.C.P.; Centeno, D.; Carvalho, F.M.; Avila, J.A.; Masoumi, M.: Improvement of tensile properties by controlling the microstructure and crystallographic data in commercial pearlitic carbon-silicon steel via quenching and partitioning (Q&P) process. *J. Mater. Res. Technol.* **23**, 845 (2023)
- Carvalho, F.M.; Centeno, D.; Tressia, G.; Avila, J.A.; Cezario, F.E.M.; Márquez-Rossy, A.; Ariza, E.A.; Masoumi, M.: Development of a complex multicomponent microstructure on commercial carbon-silicon grade steel by governing the phase transformation mechanisms to design novel quenching and partitioning processing. *J. Mater. Res. Technol.* **18**, 4590 (2022)
- Ganesh, P.; Sundar, R.; Kumar, H.; Kaul, R.; Ranganathan, K.; Hedao, V.; Tiwari, P.; Kukreja, L.M.; Oak, S.M.; Dasari, S.; Raghavendra, G.: Studies on laser peening of spring steel for automotive applications. *Opt. Lasers Eng.* **50**(5), 678 (2012)



17. Prabhakaran, S.; Kalainathan, S.: Compound technology of manufacturing and multiple laser peening on microstructure and fatigue life of dual-phase spring steel. *Mater. Sci. Eng. A* **674**, 634 (2016)
18. Nkhoma, R.; Annan, K.A.; Siyasiya, C.: Effect of adding Cr, Ni and Mo on quench and temper microstructure and mechanical properties of a Si-Mn spring steel. *Mater. Today Proc.* **56**, 1629 (2022)
19. Lin, S.; Borgenstam, A.; Stark, A.; Hedström, P.: Effect of Si on bainitic transformation kinetics in steels explained by carbon partitioning, carbide formation, dislocation densities, and thermodynamic conditions. *Mater Charact* **185**, 111774 (2022)
20. Ning, D.; Dai, C.R.; Wu, J.L.; Wang, Y.D.; Wang, Y.Q.; Jing, Y.; Sun, J.: Carbide precipitation and coarsening kinetics in low carbon and low alloy steel during quenching and subsequently tempering. *Mater Charact* **176**, 111111 (2021). <https://doi.org/10.1016/j.matchar.2021.111111>
21. Santofimia, M.J.; Caballero, F.G.; Capdevila, C.; García-Mateo, C.; García De Andrés, C.: New model for the overall transformation kinetics of bainite Part 2: Validation. *Mater. Trans.* **47**(10), 2473 (2006)
22. Varshney, A.; Sangal, S.; Pramanick, A.K.; Mondal, K.: On the extent of transformation of austenite to bainitic ferrite and carbide during austempering of high Si steel for prolonged duration and its effect on mechanical properties. *Mater. Sci. Eng. A* **793**, 139764 (2020)
23. Shen, Y.F.; Qiu, L.N.; Sun, X.; Zuo, L.; Liaw, P.K.; Raabe, D.: Effects of retained austenite volume fraction, morphology, and carbon content on strength and ductility of nanostructured TRIP-assisted steels. *Mater. Sci. Eng. A* **636**, 551 (2015)
24. Ariza, E.A.; Nishikawa, A.S.; Goldenstein, H.; Tschiptschin, A.P.: Characterization and methodology for calculating the mechanical properties of a TRIP-steel submitted to hot stamping and quenching and partitioning (Q&P). *Mater. Sci. Eng. A* **671**, 54 (2016)
25. Tan, X.; Lu, W.; Rao, X.: Effect of ultra-fast heating on microstructure and mechanical properties of cold-rolled low-carbon low-alloy Q&P steels with different austenitizing temperature. *Mater Charact* **191**, 112086 (2022)
26. Tan, X.; Xu, Y.; Yang, X.; Liu, Z.; Wu, D.: Effect of partitioning procedure on microstructure and mechanical properties of a hot-rolled directly quenched and partitioned steel. *Mater. Sci. Eng. A* **594**, 149 (2014)
27. Srinivasan, G.R.; Hepworth, M.T.: The crystallography of the bainite transformation in beta brass. *Acta Metall.* **19**(10), 1121 (1971)
28. Rangaswamy, P.; Scherer, C.P.; Bourke, M.A.M.: Experimental measurements and numerical simulation of stress and microstructure in carburized 5120 steel disks. *Mater. Sci. Eng. A* **298**(1–2), 158 (2001)
29. Katemi RJ (2019). Influence of carbonitriding process on phase transformation during case hardening, retained austenite and residual stresses (Doctoral dissertation, Universität Bremen)
30. Fleißner-Rieger, C.; Tunes, M.A.; Gammer, C.; Jörg, T.; Pfeifer, T.; Musi, M.; Mendez-Martin, F.; Clemens, H.: On the existence of orthorhombic martensite in a near- α titanium base alloy used for additive manufacturing. *J. Alloys Compd.* **897**, 163155 (2022)
31. Masumura, T.; Inami, K.; Matsuda, K.; Tsuchiyama, T.; Nanba, S.; Kitahara, A.: Quantitative evaluation of dislocation density in as-quenched martensite with tetragonality by X-ray line profile analysis in a medium-carbon steel. *Acta Mater.* **234**, 118052 (2022)
32. Lu, Y.; Yu, H.; Sisson, R.D.: The effect of carbon content on the c/a ratio of as-quenched martensite in Fe-C alloys. *Mater. Sci. Eng. A* **700**, 592 (2017)
33. Beausir B, Fundenberger JJ (2017) Analysis Tools for Electron and X-ray diffraction, ATEX - software, Université de Lorraine - Metz
34. Klinger, M.; Jäger, A.: Crystallographic Tool Box (CrysTBox): Automated tools for transmission electron microscopists and crystallographers. *J. Appl. Crystallogr.* **48**(6), 2012–2018 (2015). <https://doi.org/10.1107/S1600576715017252>
35. Klinger, M.: More features, more tools, more CrysTBox. *J. Appl. Crystallogr.* **50**, 1226 (2017)
36. De Knijf, D.; Petrov, R.; Föjér, C.; Kestens, L.A.I.: Effect of fresh martensite on the stability of retained austenite in quenching and partitioning steel. *Mater. Sci. Eng. A* **615**, 107 (2014)
37. Stock, R.; Pippin, R.: RCF and wear in theory and practice-The influence of rail grade on wear and RCF. *Wear* **271**(1–2), 125 (2011)
38. Pereira, H.B.; Ariza-Echeverri, E.A.; Centeno, D.; Souza, S.; Bauri, L.F.; Manfrinato, M.; Masoumi, M.; Alves, L.H.; Goldenstein, H.: Effect of pearlitic and bainitic initial microstructure on cementite spheroidization in rail steels. *J. Mater. Res. Technol.* **23**, 1903 (2023)
39. Koistinen, D.; Marburger, R.E.: A general equation prescribing the extent of the austenite-martensite transformation in pure iron-carbon alloys and plain carbon steels. *Acta Metall.* **7**(1), 59 (1959)
40. Otun, K.O.; Yao, Y.; Liu, X.; Hildebrandt, D.: Synthesis, structure, and performance of carbide phases in Fischer-Tropsch synthesis: A critical review. *Fuel* **296**, 120689 (2021)
41. Zhang, K.; Zhu, M.; Lan, B.; Liu, P.; Li, W.; Rong, Y.: The mechanism of high-strength quenching-partitioning-tempering martensitic steel at elevated temperatures. *Crystals* **9**(2), 94 (2019)
42. Nový, Z.; Salvetr, P.; Kotous, J.; Motyčka, P.; Gokhman, A.; Donik, Č.; Džugan, J.: Enhanced spring steel's strength using strain assisted tempering. *Materials (Basel)*. **15**(20), 1 (2022)
43. Bhadeshia, H.K.D.H.; Chinthia, A.R.; Lenka, S.: Critical Assessment 34: Are χ (Hägg), η and ϵ carbides transition-phases relative to cementite in steels? *Mater. Sci. Technol.* **35**(11), 1301 (2019)
44. Liu, X.W.; Cao, Z.; Zhao, S.; Gao, R.; Meng, Y.; Zhu, J.X.; Rogers, C.; Huo, C.F.; Yang, Y.; Li, Y.W.; Wen, X.D.: Iron carbides in Fischer-Tropsch synthesis: theoretical and experimental understanding in epsilon-iron carbide phase assignment. *J. Phys. Chem. C* **121**(39), 21390 (2017)
45. Wu, Y.X.; Sun, W.W.; Gao, X.; Styles, M.J.; Arlazarov, A.; Hutchinson, C.R.: The effect of alloying elements on cementite coarsening during martensite tempering. *Acta Mater.* **183**, 418 (2020)
46. Wu, Y.X.; Sun, W.W.; Styles, M.J.; Arlazarov, A.; Hutchinson, C.R.: Cementite coarsening during the tempering of Fe-C-Mn martensite. *Acta Mater.* **159**, 209 (2018)
47. Morsdorf, L.; Kashiwar, A.; Kübel, C.; Tasan, C.C.: Carbon segregation and cementite precipitation at grain boundaries in quenched and tempered lath martensite. *Mater. Sci. Eng. A* **862**, 144369 (2023). <https://doi.org/10.1016/j.msea.2022.144369>
48. Ravi, A.M.; Navarro-López, A.; Sietsma, J.; Santofimia, M.J.: Influence of martensite/austenite interfaces on bainite formation in low-alloy steels below Ms. *Acta Mater.* **188**, 394 (2020)
49. Ayenampudi, S.; Celada-Casero, C.; Sietsma, J.; Santofimia, M.J.: Microstructure evolution during high-temperature partitioning of a medium-Mn quenching and partitioning steel. *Materialia*. **8**, 100492 (2019)
50. Baltušnikas, A.; Levinskas, R.: XRD Analysis of Carbide Phase in Heat Resistant Steels. *Mater. Sci.* **12**(3), 192–198 (2006)
51. Dong, H.Y.; Hu, C.Y.; Wu, G.H.; Wu, K.M.; Misra, R.D.K.: Effect of nickel on hardening behavior and mechanical properties of nanostructured bainite-austenite steels. *Mater. Sci. Eng. A* **817**, 141410 (2021)
52. Dragomir, I.C.; Li, D.S.; Castello-Branco, G.A.; Garmestani, H.; Snyder, R.L.; Ribarik, G.; Ungar, T.: Evolution of dislocation density and character in hot rolled titanium determined by X-ray diffraction. *Mater Charact* **55**(1), 66 (2005)
53. Alvarez, M.A.; Santisteban, J.R.; Vizcaíno, P.; Ribárik, G.; Ungar, T.: Quantification of dislocations densities in zirconium hydride by X-ray line profile analysis. *Acta Mater.* **117**, 1 (2016)
54. Ruiz-Jimenez, V.; Kuntz, M.; Sourmail, T.; Caballero, F.G.; Jimenez, J.A.; Garcia-Mateo, C.: Retained austenite destabilization



- during tempering of low-temperature bainite. *Appl. Sci.* **10**(24), 1 (2020)
55. Tanaka, T.; Maruyama, N.; Nakamura, N.; Wilkinson, A.J.: Tetragonality of Fe-C martensite – a pattern matching electron backscatter diffraction analysis compared to X-ray diffraction. *Acta Mater.* **195**, 728 (2020)
56. Kumar, S.; Singh, S.B.: Evolution of microstructure during the “quenching and partitioning (Q&P)” treatment. *Materialia.* **18**, 101135 (2021)
57. Morsdorf, L.; Tasan, C.C.; Ponge, D.; Raabe, D.: 3D structural and atomic-scale analysis of lath martensite: effect of the transformation sequence. *Acta Mater.* **95**, 366 (2015)
58. Bhadeshia, H.K.D.H.: Bainite in steels: transformation, microstructure and properties, p. 237–276. IOM, London (2001)
59. Das-Bakshi, S.; Sinha, D.; Ghosh-Chowdhury, S.: Anisotropic broadening of XRD peaks of α' -Fe: Williamson-Hall and Warren-Averbach analysis using full width at half maximum (FWHM) and integral breadth (IB). *Mater Charact* **142**, 144 (2018)
60. Gao, G.; Liu, R.; Wang, K.; Gui, X.; Misra, R.D.K.; Bai, B.: Role of retained austenite with different morphologies on sub-surface fatigue crack initiation in advanced bainitic steels. *Scr. Mater.* **184**, 12 (2020)
61. Zhao, S.; Min, N.; Li, W.: Formation of Widmanstätten ferrite and grain boundary ferrite in a hypereutectoid pearlitic steel. *Metals (Basel).* **12**(3), 1 (2022)
62. Li, X.L.; Lei, C.S.; Tian, Q.; Deng, X.T.; Chen, L.; Gao, P.L.; Du, K.P.; Du, Y.; Yu, Y.G.; Wang, Z.D.; Misra, R.D.K.: Nanoscale cementite and microalloyed carbide strengthened Ti bearing low carbon steel plates in the context of newly developed ultrafast cooling. *Mater. Sci. Eng. A* **698**, 268 (2017)
63. Seret, A.; Moussa, C.; Bernacki, M.; Signorelli, J.; Bozzolo, N.: Estimation of geometrically necessary dislocation density from filtered EBSD data by a local linear adaptation of smoothing splines. *J. Appl. Crystallogr.* **52**(3), 548 (2019)
64. Read, W.T.; Shockley, W.: Dislocation models of crystal grain boundaries. *Phys. Rev.* **78**(3), 275 (1950)
65. Gaudez, S.; Teixeira, J.; Denis, S.; Geandier, G.; Allain, S.Y.P.: Martensite and nanobainite transformations in a low alloyed steel studied by in situ high energy synchrotron diffraction. *Mater Charact* **185**, 111740 (2022)
66. Li, S.; Zhu, G.; Kang, Y.: Effect of substructure on mechanical properties and fracture behavior of lath martensite in 0.1C–1.1Si–1.7Mn steel. *J. Alloys Compd.* **675**, 104 (2016)
67. Brown, C.S.; Speer, J.G.; De Moor, E.: Influence of retained austenite on abrasive wear performance of bainitic steels. *Wear* **522**, 204720 (2023). <https://doi.org/10.1016/j.wear.2023.204720>

